



**UNIVERSIDAD DE INVESTIGACIÓN DE
TECNOLOGÍA EXPERIMENTAL YACHAY**

Escuela de Ciencias Químicas e Ingeniería

**TÍTULO: Metallic oxides, sulfides, and carbon-based materials
as hole extracting layers in organic photovoltaic devices**

Trabajo de integración curricular presentado como requisito para la
obtención del título de Química

Autor:

Anrango Camacho Cinthya Anabel

Tutor:

Dr. Palma Cando Alex Uriel

Cotutor:

Dr. Frontana Uribe Bernardo Antonio

Urcuquí, abril 2021

SECRETARÍA GENERAL
(Vicerrectorado Académico/Cancillería)
ESCUELA DE CIENCIAS QUÍMICAS E INGENIERÍA
CARRERA DE QUÍMICA
ACTA DE DEFENSA No. UITEY-CHE-2021-00002-AD

A los 11 días del mes de mayo de 2021, a las 10:00 horas, de manera virtual mediante videoconferencia, y ante el Tribunal Calificador, integrado por los docentes:

Presidente Tribunal de Defensa	Dra. LOPEZ GONZALEZ, FLORALBA AGGENY , Ph.D.
Miembro No Tutor	Dr. SAUCEDO VAZQUEZ, JUAN PABLO , Ph.D.
Tutor	Dr. PALMA CANDO, ALEX URIEL , Ph.D.

El(la) señor(ita) estudiante **ANRANGO CAMACHO, CINTHYA ANABEL**, con cédula de identidad No. **1726396375**, de la **ESCUELA DE CIENCIAS QUÍMICAS E INGENIERÍA**, de la Carrera de **QUÍMICA**, aprobada por el Consejo de Educación Superior (CES), mediante Resolución **RPC-SO-39-No.456-2014**, realiza a través de videoconferencia, la sustentación de su trabajo de titulación denominado: **METALIC OXIDES, SULFIDES AND CARBON-BASED MATERIALS AS HOLE EXTRACTING LAYERS IN ORGANIC PHOTOVOLTAIC DEVICES**, previa a la obtención del título de **QUÍMICO/A**.

El citado trabajo de titulación, fue debidamente aprobado por el(los) docente(s):

Tutor	Dr. PALMA CANDO, ALEX URIEL , Ph.D.
--------------	-------------------------------------

Y recibió las observaciones de los otros miembros del Tribunal Calificador, las mismas que han sido incorporadas por el(la) estudiante.

Previamente cumplidos los requisitos legales y reglamentarios, el trabajo de titulación fue sustentado por el(la) estudiante y examinado por los miembros del Tribunal Calificador. Escuchada la sustentación del trabajo de titulación a través de videoconferencia, que integró la exposición de el(la) estudiante sobre el contenido de la misma y las preguntas formuladas por los miembros del Tribunal, se califica la sustentación del trabajo de titulación con las siguientes calificaciones:

Tipo	Docente	Calificación
Tutor	Dr. PALMA CANDO, ALEX URIEL , Ph.D.	9,9
Presidente Tribunal De Defensa	Dra. LOPEZ GONZALEZ, FLORALBA AGGENY , Ph.D.	10,0
Miembro Tribunal De Defensa	Dr. SAUCEDO VAZQUEZ, JUAN PABLO , Ph.D.	10,0

Lo que da un promedio de: **10 (Diez punto Cero)**, sobre 10 (diez), equivalente a: **APROBADO**

Para constancia de lo actuado, firman los miembros del Tribunal Calificador, el/la estudiante y el/la secretario ad-hoc.

Certifico que en cumplimiento del Decreto Ejecutivo 1017 de 16 de marzo de 2020, la defensa de trabajo de titulación (o examen de grado modalidad teórico práctica) se realizó vía virtual, por lo que las firmas de los miembros del Tribunal de Defensa de Grado, constan en forma digital.

ANRANGO CAMACHO, CINTHYA ANABEL
Estudiante

Dra. LOPEZ GONZALEZ, FLORALBA AGGENY , Ph.D.
Presidente Tribunal de Defensa

FLORALBA
 AGGENY LOPEZ
 GONZALEZ

Digitally signed by
 FLORALBA AGGENY
 LOPEZ GONZALEZ
 Date: 2021.05.11 12:19:56
 -05'00'

Dr. PALMA CANDO, ALEX URIEL , Ph.D.
Tutor



Firmado electrónicamente por:
**ALEX URIEL
PALMA CANDO**

Dr. SAUCEDO VAZQUEZ, JUAN PABLO , Ph.D.
Miembro No Tutor

JUAN PABLO SAUCEDO VAZQUEZ
Firmado digitalmente por JUAN PABLO SAUCEDO VAZQUEZ
Nombre de reconocimiento (DN): c=EC,
ou=BANCO CENTRAL DEL ECUADOR,
ou=ENTIDAD DE CERTIFICACION DE
INFORMACION FIDEL Y-SIGUITS,
serialNumber=c=COOR26795, cn=JUAN
PABLO SAUCEDO VAZQUEZ
Fecha: 2021.05.11 12:58:43 -05'00'

CIFUENTES TAFUR, EVELYN CAROLINA
Secretario Ad-hoc

EVELYN CAROLINA CIFUENTES TAFUR
Digitally signed by
EVELYN CAROLINA
CIFUENTES TAFUR
Date: 2021.05.11
12:17:02 -05'00'

AUTORÍA

Yo, Cinthya Anabel Anrango Camacho, con cédula de identidad 1726396375, declaro que las ideas, juicios, valoraciones, interpretaciones, consultas bibliográficas, definiciones y conceptualizaciones expuestas en el presente trabajo, así como, los procedimientos y herramientas utilizadas en la investigación, son de absoluta responsabilidad del autor del trabajo de integración curricular. Así mismo, me acojo a los reglamentos internos de la Universidad de Investigación de Tecnología Experimental Yachay.

Urcuquí, abril 2021



Cinthya Anabel Anrango Camacho

CI: 1726396375

AUTORIZACIÓN DE PUBLICACIÓN

Yo, Cinthya Anabel Anrango Camacho, con cédula de identidad 1726396375, cedo a la Universidad de Investigación de Tecnología Experimental Yachay, los derechos de publicación de la presente obra, sin que deba haber un reconocimiento económico por este concepto. Declaro además que el texto del presente trabajo de titulación no podrá ser cedido a ninguna empresa editorial para su publicación u otros fines, sin contar previamente con la autorización escrita de la Universidad.

Así mismo, autorizo a la Universidad que realice la digitalización y publicación de este trabajo de integración curricular en el repositorio virtual, de conformidad a lo dispuesto en el Art. 144 de la Ley Orgánica de Educación Superior.

Urququí, abril 2021



Cinthya Anabel Anrango Camacho

CI: 1726396375

*To my parents José and Lilia and my brother Michael
for their unconditional support and love.*

Acknowledgments

I would like to express my gratitude to all those who gave their support to complete this thesis.

First of all, I would like to thank God for the health and my dear parents José and Lilia and brother Michael for their unconditional love, moral support, and patience. Also, I would like to thank my beloved Álvaro, whose love and help have been vital in my personal and academic growth.

Thanks to the projects CHEM19_17 YT and PAPIIT IN208919 DGAPA UNAM.

Thanks to my friend and research partner, Karla, with whom I developed this research project.

I would like to express my sincere thanks to my supervisor, and professor Alex Palma, whose help, suggestions, and advice helped me in the research and writing of this thesis.

Finally, thanks to my co-advisor Dr. Bernardo A. Frontana and the members of the jury, Dr. Juan Pablo Saucedo and Dra. Floralba Lopez for the comments and suggestions in the present research work.

Resumen

La mayor parte de la generación de energía utiliza combustibles fósiles, que liberan gases nocivos de dióxido de carbono a la atmósfera terrestre. Una alternativa sostenible y rentable para satisfacer la demanda energética de la población humana son las celdas solares orgánicas (OSCs por sus siglas en inglés). Dentro de los avances en los OSCs, el desarrollo de materiales de interfaz eficientes y estables es importante para lograr un alto rendimiento, estabilidad a largo plazo, bajos costos y una aplicabilidad más amplia. Los materiales inorgánicos y aquellos a base de carbono muestran una función de trabajo adecuada, propiedades ópticas/electrónicas sintonizables, estabilidad a la humedad y fácil procesamiento de la solución, lo que los hace atractivos como capas extractora de agujeros (HELs por sus siglas en inglés) para OSCs. Esta revisión analiza el progreso reciente en óxidos metálicos, sulfuros metálicos y materiales a base de carbono como HELs en OSCs durante los últimos cinco años. Para facilitar la fabricación y la rentabilidad de las OSCs, se utilizan precursores procesados en solución para preparar HELs de óxidos metálicos (MoO_3 , WO_x , VO_x , NiO_x , CuO_x), sulfuros metálicos (MoS , WS , NiS , CuS) y nanocarbonos (GO, CNT, CQD). Actualmente, la investigación sobre los precursores en solución aún está en curso. Los esfuerzos en investigación y tecnología han optimizado los métodos de preparación y deposición. Las estrategias de dopaje, formación de compositos/híbridos, y modificaciones también han ajustado las propiedades ópticas/eléctricas de los óxidos metálicos, sulfuros metálicos y nanocarbonos como HELs para obtener OSCs eficientes y estables. Esta revisión destaca el impacto de la estructura, la composición y las condiciones de procesamiento de los materiales inorgánicos y nanocarbonos como HEL en las OSCs convencionales e invertidas. Estudios posteriores en la ingeniería de capas de interfaz y su relación con el mecanismo de movilidad de los agujeros son indispensables para mejorar la eficiencia de los OSCs.

Palabras clave:

Celdas solares orgánicas, capas de extracción de agujeros, eficiencia, estabilidad, óxidos metálicos, sulfuros metálicos, nanocarbonos

Abstract

Most of the power generation uses fossil fuels, releasing harmful carbon dioxide gases into the Earth's atmosphere. A sustainable and cost-effective alternative to fulfill the human population's energy demand is organic solar cells (OSCs). Within OSC's advancements, the development of efficient and stable interface materials is essential to achieve high performance, long-term stability, low costs, and broader applicability. Inorganic and carbon-based materials show a suitable work function, tunable optical/electronic properties, stability to the moisture presence, and facile solution processing, making them attractive as hole extracting layers (HELs) for OSCs. This review looks at the recent progress in metal oxides, metal sulfides, and nanocarbon materials as HELs in OSCs over the past five years. To facilitate the manufacture and profitability of OSCs, it uses solution-processed precursors for preparing HELs of metal oxides (MoO_3 , WO_x , VO_x , NiO_x , CuO_x), metal sulfides (MoS , WS , NiS , CuS), and nanocarbon materials (GO, CNTs, CQDs). Currently, research on precursors in solution is still underway. The endeavors in research and technology have optimized the preparation and deposition methods. Strategies of doping, composite/hybrid formation, and modifications have also tuned the optical/electrical properties of metal oxides, metal sulfides, and nanocarbon materials as HELs to obtain efficient and stable OSCs. This review highlights the impact of structure, composition, and processing conditions of inorganic and nanocarbon materials as HELs in conventional and inverted OSCs. Further studies in the engineering of interface layers and their relationship with the mechanism of hole mobility are highly needed to improve OSCs' efficiency.

Keywords:

Organic solar cells, hole extracting layers, efficiency, stability, metal oxides, metal sulfides, nanocarbon materials.

ABBREVIATIONS AND ACRONYMS

(NH₄)₂MoO₄	Ammonium molybdate
AFM	Atomic force microscope
AHM	Ammonium heptamolybdate
a-MWNTs	Amino-functionalized multi-walled carbon nanotubes
BHJ	Bulk heterojunction
CoO_x	Cobalt oxide
CTAB	Cetyltrimethylammonium bromide
Cu₂CdSnS₄	Copper cadmium tin sulfide
CuBr	Copper bromide
CuCrO₂	Copper chromium oxide
CuI₃	Copper iodide
CuO_x	Copper oxide
CuSCN	Copper thiocyanate
CuS_x	Copper sulfide
DC	Direct current
DMF	Dimethylformamide
EQE	External quantum efficiency
F₄TCNQ	Tetrafluorotetracyanoquino-dimethane
FF	Fill factor
GO	Graphene oxide
GQDs	Graphene quantum dots
H₂O₂	Hydrogen peroxide
HEL	Hole extracting layer
HOMO	High occupied molecular orbital
H_yMoO_{3-x}	Hydrogenated molybdenum oxide
ITO	Indium tin oxide
J_{sc}	Short circuit current
LSRP	Localized surface resonance plasmon
LUMO	Lowest unoccupied molecular orbital
MoO₃	Molybdenum oxide
MoS₂	Molybdenum sulfide
MW	Microwave
NH₄OH	Ammonium hydroxide

NiO_x	Nickel oxide
NiS_x	Nickel sulfide
NPs	Nanoparticles
OLED	Organic light emitting diodes
OSCs	Organic solar cells
PANI	Polyaniline
PCE	Power conversion efficiency
PEDOT:PSS	Poly(3,4-ethylenedioxythiophene)-poly(styrene sulfonate)
PEG	Polyethylene glycol
PMC	Polynuclear metal-oxo clusters
PTCDA	3,4,9,10-perylenetetracarboxylic dianhydride
R_s	Series resistance
R_{sh}	Shunt resistance
RMS	Root mean square
SEM	Scanning electron microscopy
SILAR	Successive ionic layer adsorption and reaction
SWCNTs	Single-walled carbon nanotubes
UVO	Ultraviolet ozone
V_{oc}	Open circuit voltage
VO_x	Vanadium oxide
WF	Work function
WO_x	Tungsten oxide
WS_x	Tungsten sulfide

Index

AUTORÍA.....	v
AUTORIZACIÓN DE PUBLICACIÓN	vi
Acknowledgments.....	viii
Resumen.....	ix
Abstract.....	x
ABBREVIATIONS AND ACRONYMS	xi
CHAPTER 1: Introduction to Hole Extracting Layers in Organic Solar Cells.....	1
1.1 Introduction.....	1
1.2 Organic Solar Cells	1
1.2.1 Structure and architecture of Organic Solar Cells	2
1.2.2 Operating Principles.....	3
1.2.3 Methods for fabrication of Organic Solar Cells.....	3
1.2.4 Characterization of Organic Solar Cells	4
1.2.5 Interfacial Extracting Layers.....	6
1.3 Problem Statement	7
1.4 Objectives.....	8
1.4.1 General Objective	8
1.4.2 Specific Objectives	8
CHAPTER 2: State-of-the-Art Review	9
2.1 Inorganic Hole Extracting Layers	9
2.1.1 Metal oxides.....	9
2.1.2 Metal sulfides.....	23
2.1.3 Miscellaneous	26
2.2 Nanocarbon Hole Extracting Layers	33
2.2.1 Graphene Oxide	33
2.2.2 Graphene Quantum Dots.....	37

2.2.3	Carbon Nanotubes.....	38
2.2.4	Single-Walled Carbon Nanotubes.....	38
CHAPTER 3: Conclusions and Recommendations.....		42
References		44

CHAPTER 1: Introduction to Hole Extracting Layers in Organic Solar Cells

1.1 Introduction

Global energy demand grows as fast as the need to improve the standards of humanity's living¹; for example, energy demand for economic growth in Iran increased by 20% from 2006 to 2011². In the mid-1970s, the energy crisis in the United States from the depletion of fossil fuels promoted renewable energy sources and energy storage strategies^{3,4}. In the 1980s, the risks attributed to tons of carbon dioxide emissions from burning fossil fuels prompted policies that will safeguard the environment^{5,6}. To reduce atmospheric carbon dioxide, "a greenhouse gas", carbon sequestration processes have been explored; however, these result most expensive and energy-intensive^{7,8}. Thus, renewable and sustainable energy sources such as wind, biomass, solar thermal, hydroelectric, ocean, geothermal, and photovoltaic renewable energy sources are crucial to meet future energy needs.

Solar energy has enough power capacity to satisfy the whole world's demand^{9,10}. According to Luqman *et al.*¹¹, the amount of solar energy irradiated at the Earth's atmosphere goes from 200 to 250 Wm⁻² per day, of which ca. 70% is available for conversion into power generation^{12,13}. Research on solar energy technology, which aims to convert sunlight directly into electrical energy, is vital to switch into low-carbon energy^{14,15}. The intense developments concerning solar energy have boosted the investigations to optimize the efficiency and stability of emerging photovoltaic technology, such as dye-sensitized solar cells (DSSCs), organic solar cells (OSCs), perovskite solar cells (PSC), quantum dot solar cells (QDSC), and so on, of which OSCs are one of the most promising¹⁶⁻²².

1.2 Organic Solar Cells

OSCs are based on organic semiconductors as active layers with unique advantages to achieve low-cost renewable energy harvesting owing to their material and manufacturing advances^{23,24}. The large-area solution processing, lightweight, flexibility, tunable transparency, short energy payback times, and greener manufacturing have drawn attention to OSCs' great potential in diverse applications, such as battery chargers^{25,26}. In the last ten years, extensive research and development have been conducted at OSCs in improving lifetimes (7-10 years) and the power conversion efficiencies (PCE) above 10% in roll-to-roll industrial manufacturing for the

commercial market^{27–30}. Since Kearns and Calvin's pioneering work on OSCs in 1958, one significant breakthrough in solar energy technology has been the efficient electron transfer between a conjugated polymer and fullerene derivative^{31,32}. It encouraged the interest in the light-harvesting of OSCs from the structure device until the materials used for their construction^{32–35}.

1.2.1 Structure and architecture of Organic Solar Cells

A conventional OSC consists of an active layer sandwiched between two electrodes with their respective extracting layers to ensure mobility, collection, and transport of the charge carriers³⁶. At the bottom, the anode electrode is a transparent conductive oxide, such as indium tin oxide (ITO), and at the top, the cathode is a low work function (WF) metal, such as Ca and Al, see Figure 1a³⁷.

The organic solar cells based on two organic semiconductors in the active layer can acquire two architectures: the bilayer and the bulk heterojunction devices. Tang *et al.* presented the sequentially stacking of donor and acceptor semiconductors to form the bilayer planar heterojunction in 1986³³. However, it has limitations, such as the small surface area between the donor/acceptor interface and the poor excitons' dissociation. Then, the introduction of bulk heterojunction (BHJ) devices in 1990 solved bilayer devices' issues³⁵. It involves mixing donor and acceptor materials in the bulk body of an OSC to reduce phase separation. Donor and acceptor domains are twice the size of the exciton diffusion length (~10 nm). To expand the active layer's absorption range, tandem OSCs have been proposed to stack two single-junctions with different absorption ranges^{38,39}. According to the charge flow direction, OSCs can be divided into conventional and inverted devices (see Figure 1a,b)⁴⁰.

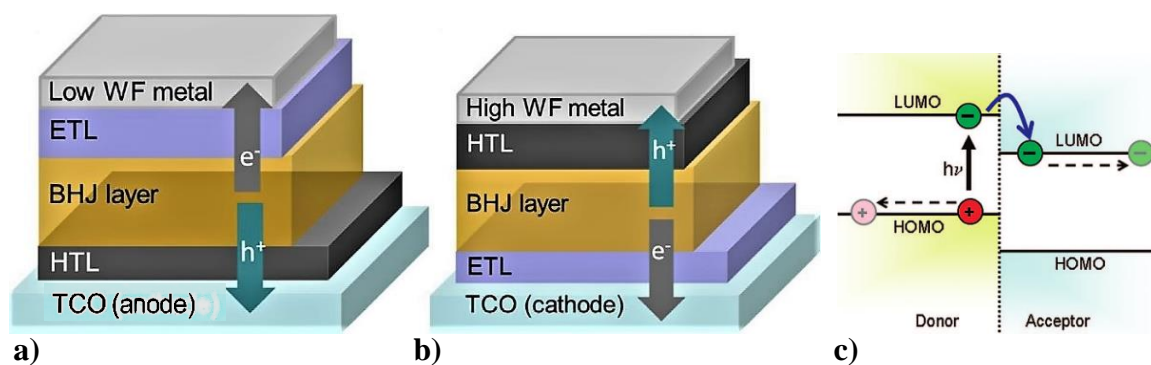


Figure 1. (a) Schematic device conventional structure; (b) inverted structure [41]. (c) The simplified view of the operating principle in the active layer. Reprinted with permission from [42]. Copyright 2010 American Chemical Society.

1.2.2 *Operating Principles*

Under light irradiation, photons are absorbed in the active layer to form excited states, called “excitons”, which are bound electron-hole pairs. Excitons diffuse towards donor/acceptor interface and separate into holes and electrons in the highest occupied molecular orbital (HOMO) of the donor and the lowest unoccupied molecular orbital (LUMO) of the acceptor, see Figure 1c. Then, the separated charge carriers are transported and collected at the electrodes to supply the photocurrent⁴³.

1.2.3 *Methods for fabrication of Organic Solar Cells*

Currently, there is an excellent development of cost-effective low-temperature deposition strategies for industrial scaling to avoid the traditional vacuum method used in the manufacture of OSCs.

1.2.3.1 Casting

It casts the material dissolved in liquid form in a solvent on the underlying substrate, followed by drying. Spray casting solves the lack of control in film morphology and uniformity⁴⁴.

1.2.3.2 Spin Coating

The spin coating technique is the most common deposition method of OSCs by its high reproducibility in film thickness and morphology, but neither large area applicability nor in film patterning. It applies the spinning at a certain rotation speed of the substrate to dry the deposited liquid material⁴⁵.

1.2.3.3 Electrodeposition

Through an electric field, electrodeposition allows depositing polymers and inorganic materials, particularly at the cathode surface, to avoid an oxidative process at the substrate surface. The control on deposition has broader applicability for the formation of composites and hybrids⁴⁶.

1.2.3.4 Roll-to-roll techniques

The roll-to-roll technique is usually utilized in flexible OSCs because the flexible substrate is unwound to pass through printing or coating machines, followed by rewind on a roll. It opens

the applicability for large-area production because substrates are not handled individually but instead in rolls^{47,48}.

These four deposition methods are less expensive for technological applications than vacuum deposition, without involving high temperature and pressure. Compared to the vacuum method, these techniques' solution processability offers the advantage of a continuous process such as roll-to-roll coating to avoid wasting raw material.

1.2.4 Characterization of Organic Solar Cells

The current-voltage (J-V) curve of an OSC is characterized under 1000 W/m² light of AM 1.5 solar spectrum⁴⁹. Figure 2a shows the J-V curve of an OSC under darkness and illumination conditions. The dotted curve shows the dark case, in which not photocurrent is flowing through the electrodes, just the current by the forward bias of contacts as a diode. Under light irradiation, photocurrent is generated whose efficiency (η) or power conversion efficiency (PCE) is the product of three parameters, short-circuit current density (J_{sc}), open-circuit voltage (V_{oc}), and fill factor (FF) over the incident light power density (P_{in}) as follows⁵⁰:

$$\eta = \frac{V_{oc} * J_{sc} * FF}{P_{in}} \quad (1)$$

J_{sc} relates the efficiency of the operating principle of the OSC⁵¹. J_{sc} can be obtained by the product of the photoinduced charge carrier density (n) with the charge carrier mobility (μ), where e is the elementary charge and E is the electric field, see below.

$$J_{sc} = ne\mu E \quad (2)$$

n increases by the number of absorbed photons per unit of volume, and μ by the morphology of the polymer/fullerene blend, so μ depends on the film preparation conditions. The direct incident light intensity (I) dependence of J_{sc} is also dependent on μ ⁵². The ratio of collected photogenerated charges and the number of incident photons allows having an idea of the external quantum efficiency (EQE) of the OSC.

V_{oc} is the main driving force for charge separation once exciton achieves the donor/acceptor interface^{53,54}. V_{oc} is the difference of work functions between the quasi-Fermi levels of holes ($E_{F,h}$) in the HOMO level of the donor and electrons ($E_{F,e}$) in the LUMO level of the acceptor in the BHJ under the formation of ohmic contacts with the cathode and anode (depicted as V_{oc-1} in Figure 2b). However, when a Schottky contact appears in both BHJ/electrode

interfaces, the V_{oc} will decrease and will dependent on the difference between the work functions of the two metal contacts (depicted as V_{oc-2} in Figure 2b)^{55,56}.

FF is the ratio between the maximum output power point (M_{pp}) and the maximum attainable power output ($J_{sc} * V_{oc}$), as follows⁵⁰:

$$FF = \frac{M_{pp}}{J_{sc} * V_{oc}} = \frac{J_m * V_m}{J_{sc} * V_{oc}} \quad (3)$$

M_{pp} describes the maximum power drawn from the device. M_{pp} is the product of the largest current and voltage marked as J_m and V_m (see Figure 2a)²⁶. The main factors that influence the FF are the series resistance (R_s) and the shunt resistance (R_{sh}) and their interaction determines the current flow. R_s is attributed to conductivity of electrodes, bulk heterojunction and extracting interface layers, and the contact resistance between them⁵⁷. The small R_s increases the mobility of the charge carriers and the performance of OSCs⁵⁸. R_{sh} is the current losses from the pinholes or traps in the film. R_{sh} inversely relates the leakage current density (J_{sh}) according to the following Ohm's law:

$$J_{sh} = \frac{V - J R_s}{R_{sh}} \quad (4)$$

J_{sh} is an undesirable current injected from the electrodes in the opposite direction to J_{sc} . A suitable interface morphology decreases J_{sh} and increase R_{sh} independently of the light intensities (see Figure 2c)⁵⁹. Thus, the contact quality at the active layer/electrode interface is critical to optimize FF , V_{oc} and J_{sc} . Interface films enhances all these OSC parameters because it tunes the energy level alignment at the active layer and electrodes, surface morphology, and the contact to boost the efficiency and stability⁶⁰.

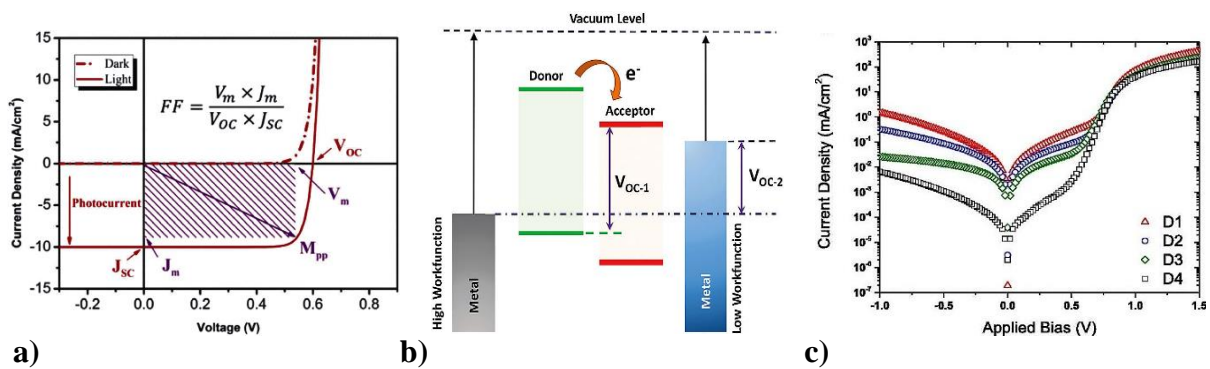


Figure 2. (a) Typical current-voltage curve. Reproduced from ref. [50] with permission from the PCCP Owner Societies. (b) open-circuit voltage. Reproduced from ref. [54] with permission from the Royal Society of

Chemistry. (c) the current-voltage response is measured in the dark, with R_{sh} ranging from low to very high. Reproduced with permission from ref. [59]. Copyright 2015 AIP Publishing LLC.

1.2.5 *Interfacial Extracting Layers*

Interfacial layers are critical components of OSCs to enhance the collection efficiency of holes and electrons toward the anode and cathode electrodes. In photovoltaic devices, including OSCs, there are barriers to charge extraction by the nonideal contact between the active layer and the electrodes⁶¹. This limited interfacial energy alignment inhibits the spontaneous charge transport, resulting in charge accumulation at the interface, thus decreasing V_{oc} , FF, and PCE⁵¹. Interfacial layers with suitable WFs contribute to match the energy levels of donor and acceptor materials with the electrodes, favoring the charge transport and stability⁶². The interfacial layers must be charge selective to avoid charge recombination at the electrodes in addition to the energy level tuning. In that sense, it has designed hole extracting layers (HELs) and electron transporting layers (ETLs), which in addition to the energy-levels requirements, increase the hole and electron mobility in the opposite direction to collect only one type of charge on each electrode⁶³.

1.2.5.1 **Hole Extracting Layers**

In the 1990s, hole extracting layers (HELs) were introduced in the organic electronics field by Tokito *et al.* when hole-injection increased from inserting vanadium, molybdenum, and ruthenium oxides as HELs in organic light-emitting diodes (OLED)⁶⁴. A hole extracting layer (HEL) 's central role is the efficient hole-extraction and transport of holes from the HEL/active interface to the anode/HEL interface, increasing power generation⁶⁵. To achieve high performance, the materials for HELs need to fulfill the following requirements: (1) high work function matched with the HOMO energy level of the donor and anode energy level; (2) transparency to increase the light absorption by the active layer; (3) high hole mobility to lower the charge accumulation and recombination; (4) large band gap to block electron carriers; and (5) chemically inert to external factors^{62,66,67}.

The first materials used as HELs in OSCs were inorganic *p*-type transition metal oxides (MoO_3 , WO_3 , NiO , Fe_3O_4) or metal sulfides (MoS_2), which showed high stability and performance⁶⁸⁻⁷². Most of them required high vacuum for deposition, which compared to organic materials, is costly to industrial and large-scale processing⁷³. Poly(3,4-ethylenedioxythiophene)-poly(styrene sulfonate) (PEDOT:PSS) is the standard conducting polymer as HEL in OSCs

because of the low costs, minimal toxicity, facile solution processing, and high WF. However, it is not stable at standard conditions by its hygroscopic nature⁷⁴. In this review, the progress about the fabrication methods and film properties of inorganic (metal oxides and sulfides) and nanocarbon materials as HELs in OSCs will be discussed, focused on solution processing conditions, deposition methods, doping, composite/hybrid formation, and modifications.

1.3 Problem Statement

The running out of fossil fuels and the global warming caused by the growing energy demand has led to a great deal of health and environmental damage^{75,76}. The nonrenewable fossil fuels energy market encouraged by the Industrial Revolution has led to 1.2 trillion tons of carbon dioxide emissions in 1800-2010⁷⁷. The high concentration of carbon dioxide gases traps the longwave radiation and allows the incident shortwave radiation from the sun to pass through the atmosphere and warm the terrestrial surface⁷⁸. This effect, known as global warming, rises continuously the Earth's surface temperature, triggering multiple harmful effects in physical, biological, and human systems. The melting of the poles, sea-level rise, floods, droughts in rivers and lakes, coastal erosion, and extreme natural disasters are attributed to the physical effects⁷⁹. In biological systems, it has prompted the death of flora and fauna in terrestrial and marine ecosystems⁸⁰. Climate change has also affected human beings destroying crops, food production, and life conditions because these three systems are related to each other^{81,82}. Even though carbon sequestration and geo-engineering mechanism are developing to mitigate the warming impact, renewable energy sources are the only one that does not compromise the environmental sustainability⁸³. Solar energy is a clean, renewable source to boost the transition out from fossil fuels to low carbon energy¹⁰. The energy radiation from sunlight within one hour meets the energy demand for an entire year⁸⁴. Bulk-heterojunction organic solar cells based on organic semiconductors are emerging as a new technology for reducing the carbon footprint and the cost of electricity production⁸⁵. Currently, organic solar cells are commercialized for building integrating semitransparent photovoltaics, representing 5% of the market⁸⁶. There is a vast development in the feedstock, architecture, processing conditions, and deposition technologies to potential organic solar cells' market. This research is focused on generating a state-of-the-art review about the advances in hole extracting layers that show great potential for enhancing the efficiency and production of organic solar cells.

1.4 Objectives

1.4.1 *General Objective*

- To analyze recent progress in inorganic (metal oxides and metal sulfides) and nanocarbon materials as the hole extracting layers in organic solar cells.

1.4.2 *Specific Objectives*

- To understand the critical role of hole extracting layers in the performance and stability of organic solar cells.
- To analyze the effect of the material properties modification on the J_{sc} , V_{oc} , FF, and its influence on PCE and stability.
- To discuss the solution deposition methods of hole extracting layers in organic solar cells in terms of costs, time consumption, and performance.

CHAPTER 2: State-of-the-Art Review

2.1 Inorganic Hole Extracting Layers

2.1.1 Metal oxides

2.1.1.1 Molybdenum Oxide

MoO_x is an *n*-type material with a valence band edge around 2.5-3 eV below the Fermi level and a conduction band closer to the Fermi level⁶⁵. MoO₃ has a high work function (WF=6.9 eV) and conductivity of $1.2 \times 10^{-7} \text{ Sm}^{-1}$ due to the different states of O and the multivalence of Mo in its three crystal phases (α -MoO₃, β -MoO₃, h-MoO₃)⁸⁷⁻⁸⁹. MoO₃ is a promising HEL due to its electronic structure, transparency, conductivity, and stability enhance the hole extraction and thus the efficiency of OSCs, compared to PEDOT:PSS⁹⁰. Lee *et al.* reported that MoO_x HEL-based OSC is more stable at a high operating temperature near 300-420 K than PEDOT:PSS⁹¹. Therefore, there is much research in strategies to optimize the solution processing methods and the film properties of MoO₃⁹²⁻⁹⁴.

Bortoti *et al.* obtained the orthorhombic phase of MoO₃ (α -MoO₃) by refluxing MoS₂ in HNO₃ and H₂SO₄ as the oxidant media, followed by 120 °C for 10 min to evaporate the solvent⁹⁵. The energy level of α -MoO₃ matched well with that of donor material P3HT, and 1.55% PCE was obtained in the structure FTO/ZnO/P3HT:PC₆₀BM/MoO₃/Ag. Ji *et al.* used ammonium heptamolybdate (AHM) as the precursor solution to prepare a solution-processed MoO₃ array on P3HT:PC₆₁BM as an active layer by ultrasonic spray coating method at 80 °C⁹⁶. The solution-processed MoO₃ micro arrays improved the charge transport between the active layer and the anode. Thus, the V_{oc} and FF increased to 0.59 V and 59.2%, and a higher PCE of 3.40% was achieved. MoO₃ is adequate to attain a high built-in potential and V_{oc} because it can suppress interfacial reactions at the HEL/BHJ interface⁹⁷.

MoO₃ nanoparticles (NPs) can be added at the interface between the active layer and the PEDOT:PSS to take advantage of the localized surface resonance plasmon (LSRP) effect of nanoparticles and the electronic structure of MoO₃⁹⁸. MoO₃ NPs increased the path length of the absorbed light and blocked the electrons flow to the anode, resulting in a higher J_{sc}, FF, and thus a PCE of 4.11% was reached over a long period of 30 days⁹⁹. The high transparency of MoO_x allows an enhanced back-reflected light into the active layer to enhance the photocurrent, as shown in the external quantum efficiency (EQE) curves (Figure 3a)¹⁰⁰.

At low temperatures of 80-200 °C, Jagadamma *et al.* prepared an alcohol-based MoO_x nanocrystalline suspension processed directly over temperature-sensitive active layers (see Figure 3b)¹⁰¹. The water-free solvent and the fine MoO_x nanocrystal diameter (<5 nm) resulted in a compact and smooth film with a thickness around ~5-10 nm. All inverted OSCs reached a PCE above 9%, retaining 90% of their efficiency after five months of aging. MoO₃ nanocrystals (NCs) with a size greater than 5 nm can form a composite of MoO_x with Ag nanowires (NWs) to lower the nanowire junction resistance by close packing Ag NWs. The Ag NWs/MoO_x composite also served as a barrier for Ag diffusion into the active layer's bulk. Wang *et al.* added AgAl NPs into MoO_x HEL to prevent the Ag diffusion by forming AlO_x¹⁰². The PTB7-Th:PC₇₁BM cell remained 60% of the initial PCE (9.28%) during 120 days.

Cong *et al.* used ammonium molybdate and citric acid in 2-methoxyethanol as the precursor to prepare MoO_x, followed by 10 vol.% of H₂O₂ form a stable conductive film¹⁰³. The presence of H₂O₂ induced oxygen vacancies to help in the polyvalence and conductivity of the MoO_x film. Jung *et al.* prepared a solution-processed MoO_x from the dissolution of MoO_x powder in ammonium hydroxide (NH₄OH) and isopropanol solvent¹⁰⁴. The Mo⁵⁺-OH bonds induced by hydroxyl radicals facilitated the charge transport with higher hole mobilities of 2.3×10⁻⁶ cm²V⁻¹s⁻¹ than PEDOT:PSS of 2.1×10⁻⁶ cm²V⁻¹s⁻¹. The gap states induced in the bandgap by the oxygen defects tuned the Fermi level of MoO_x with the highest unoccupied molecular orbital (HOMO) of PBDB-T as the donor material, showing overall improvement in FF and J_{sc} with a PCE of 10.86%.

The excess of oxygen vacancies during the film formation results in recombination sites which compromise the performance and stability of the OSC⁴¹. Kobori *et al.* improved the J_{sc} and FF when the as-deposited solution-processed MoO_x film was annealed at 160 °C for 2 min¹⁰⁵. The enhancement in the efficiency from 1.40% to 6.57% is due to the effect of surface passivation of MoO_x HEL by annealing treatment, resulting in a reduction of oxygen vacancies in the MoO_x film (Figure 3c). It helps the fabrication of OSCs with temperature-sensitive low-bandgap polymers, such as PTB7-Th:PC₇₁BM and PCPDTBT:PC₇₁BM. Li *et al.* reported that low-temperature annealing treatment could also enhance the preparation of solution-processed MoO_x films from peroxomolybdic acid organosol precursor solution at 150 °C, while also achieving passivation of the surface¹⁰⁶.

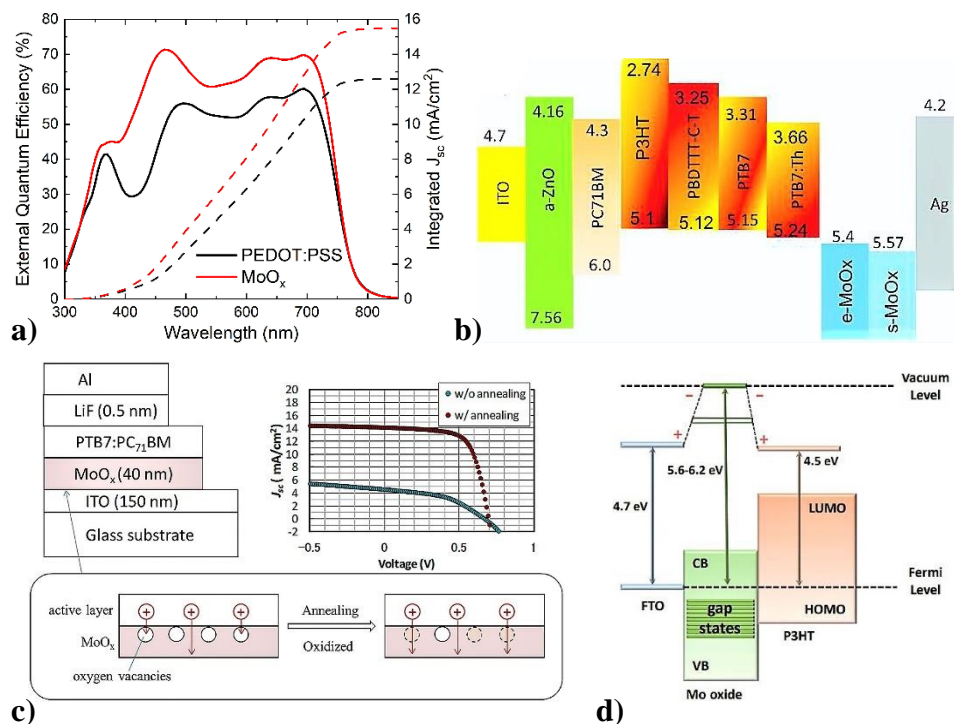


Figure 3. (a) External quantum efficiency of inverted OSCs with MoO₃ and PEDOT:PSS HELs [100]. (b) Energy level diagram of inverted OSCs with different polymer:PC₇₁BM systems. Reproduced with permission from ref. [101]. Copyright 2016, Elsevier. (c) Reduction of oxygen vacancies with annealing treatment. Reproduced with permission from ref. [105]. Copyright 2016, Elsevier. (d) Interfacial dipole formation for charge transport by gap states. Reproduced from ref. [107] with permission from the Royal Society of Chemistry.

Comparing OSCs' efficiency with no annealing, thermal annealing (100 °C), and ultraviolet (UV) annealing, the latter can keep a higher PCE of 5.4% over a longer period¹⁰⁸. UV annealing removed the adhered organic contaminants on the MoO₃ film surface by two short wave UV lights at 185 nm and 285 nm. This radiation decomposed O₃ into O₂ and active O, which oxidized and removed any organic contaminant by transformation into volatile gases. Cai *et al.* achieved a PCE of 9.27% in the PBDB-T:ITIC BHJ cell using an ultraviolet-deposited MoO₃ film¹⁰⁹.

Tan *et al.* developed a solution-processed annealing-free aqueous MoO_x for non-fullerene OSCs¹¹⁰. By adding a small amount of water to MoO₂(acac)₂, the ligand of MoO₂(acac)₂ was removed from the MoO_x film, avoiding thermal treatments and enhancing the PCE of PBDB-T-2F:Y6 cell up 17.0%.

In addition to the impurities in the precursor solution, external factors including air and oxygen create oxygen defects in the MoO_x film lattice, which change the electric properties (WF, energy levels) and the performance of the OSC^{111,112}. Soutati *et al.* reported the microwave

(MW) air annealing approach for recovering the work function (WF) in stoichiometric MoO_x and the efficiency of the FTO/MW-MoO_x/P3HT:PC₇₁BM/Al cell to 5.0%¹⁰⁷. The work function recovery resulted in forming a large interfacial dipole at the FTO/MW-MoO_x/P3HT:PC₇₁BM interfaces, favoring hole extraction via gap states, see Figure 3.

In addition to post-treatments, the film properties of the MoO₃ HEL in OSCs also improve through strategies involving doping, composite/hybrid formation, multilayers, and deposition technique.

Doping:

Chang *et al.* reported vanadium-doped MoO_x films at different ammonium metavanadate concentrations. The smallest band offset (1.13 eV) between the valence band edge of V_{0.05}MoO_x and P3HT HOMO level favored the hole transport by the lowest resistance among all V-MoO_x films¹¹³. Marchal *et al.* reported a decrease of 3 nm in the surface roughness of MoO_x HEL by adding 0.5 mol% of Zr and Sn via a combustion chemical deposition method at low temperatures¹¹⁴. The Zr and Sn atoms also covered the surface defects of MoO_x, forming an uniform and well-covered HEL film on the ITO electrode (Figure 4a). Bai *et al.* employed a small amount of *p*-type NiO_x into *n*-type MoO₃ in one step¹¹⁵. Since MoO₃:NiO_x was highly transparent and had a conduction band of 3.25 eV and a WF of 5.10 eV (Figure 4d), the MoO₃:NiO_x film was able to block electrons while enhancing the contact to charge transport toward the anode, achieving a PCE of 10.81% in PBDB-T:IT-M BHJ OSC.

Composite/Hybrid formation:

Yoon *et al.* synthesized a dual-hole transporting layer by mixing solution-processed copper iodide (CuI) and thermally evaporated MoO₃¹¹⁶. The interaction between MoO₃ and the CuI increased the forbidden gap states in the MoO₃ layer for the hole transport by forming small oxygen vacancies and Mo⁵⁺ defect states. Zhiqiu *et al.* reported a composite of copper bromide (CuBr₂) and molybdenum trioxide (MoO₃) as the HEL for OSCs¹¹⁷. CuBr optimized interfacial contact to increase charge carriers, and MoO₃ blocked electron transport, resulting in improved FF (65.20%), J_{sc} (19.65 mAcm²), and an increase in the PCE from 7.30 to 9.56%. Li *et al.* prepared CTAB-modified MoO₃ nanocomposites by adding a small amount of cetyltrimethylammonium bromide (CTAB) solution into ammonium molybdate and annealing it at 200 °C in a glovebox¹¹⁸. CTAB passivated the surface traps of MoO₃ films to avoid the

recombination sites, resulting in a film with PCEs of $5.80\pm 0.13\%$ in P3HT:ICBA and $8.34\pm 0.13\%$ in PTB7:PC₇₁BM OSCs.

The formation of polynuclear metal-oxo clusters (PMC) of tungsten/molybdenum as HELs showed PCEs of 14.3% and higher stability than PEDOT:PSS¹¹⁹. The variation in the W/Mo ratio allowed to increase the hole transport from the polymer donor (PBDBT-2F) toward anode due to the formation of an inorganic-organic charge transfer complex with a barrier-free interface. This unique characteristic of PCM clusters in OSC might promote new insights for its utility in high-performance optoelectronic devices. Kwon *et al.* also boosted the efficiency by developing an alloy of molybdenum-tungsten disulfides films as HEL to replace PEDOT:PSS efficiently¹²⁰.

Multilayers:

As it was mentioned before, Ag NPs can be incorporated into MoO₃ to enhance the electrical and optical properties of the HEL. Indeed, it can form a MoO₃/AgNPs/MoO₃ structure as HEL to improve the J_{sc} and reduce the recombination by the backscattering and surface plasmon effects of AgNPs¹²¹. Zhang *et al.* prepared a solution-processed MoO₃/AgNPs/MoO₃ (MAM) HEL in PTB7:PC70BM cells¹²². The MAM multilayer enabled an enhanced charge collection by suppressing charge recombination. The efficiency of the OSC was superior (7.68%) than the s-MoO₃ (6.72%).

The manufacture of OSCs has also been limited by the material's finite availability, such as the transparent anode electrode, ITO¹²³. An ITO-free flexible OSC obtained by Chen *et al.* used multiple layers of molybdenum oxide MoO₃/LiF/MoO₃/Ag/MoO₃ as transparent electrodes, facilitating the transmittance and charge transport¹²⁴. Lee *et al.* reported a reduced atomic percentage of In and Sn at the surface of ITO electrodes by graded sputtering of MoO₃ HELs, see Figure 4c¹²⁵. The MoO₃ graded ITO (MGI) electrode formed three regions: (i) the bottom ITO region provided high transparency (83.8%), (ii) the Mo-In-Sn-O graded interlayer, and (iii) the MoO₃ region served as the hole transporting layer.

Deposition Technique:

For thin HELs, the deposition method might cause defects or form compacted layers depending on the working conditions. Uniform s-MoO_x HELs prepared by direct current (DC) magnetron sputtering showed enhanced charge transport with a FF of 50% as the s-MoO_x film's surface

was smoother and controlled by DC in comparison to the conventional evaporated approach¹²⁶. Chaturvedi *et al.* applied a DC voltage of 1 kV during the spray deposition of MoO₃ HEL, obtaining a PCE of 2.71%¹²⁷. The applied electric field controlled both the optical and electrical properties of the thin MoO₃ film. Dong *et al.* used a laser-assisted method to obtain a hydrogenated molybdenum oxide H_yMoO_{3-x} film for flexible OSCs (see Figure 4b)¹²⁸. By controlling the energy of KrF laser ($\lambda = 248$ nm) during the irradiation of photons on the AHM precursor solution, the work function (5.6 eV) and the hole transport of H_yMoO_{3-x} film increased, allowing higher PTB7:PC₇₀BM cell performance, see Table 1. The laser processing time is only 30 ns, so it is suitable in time and economy compared to the thermal evaporation method.

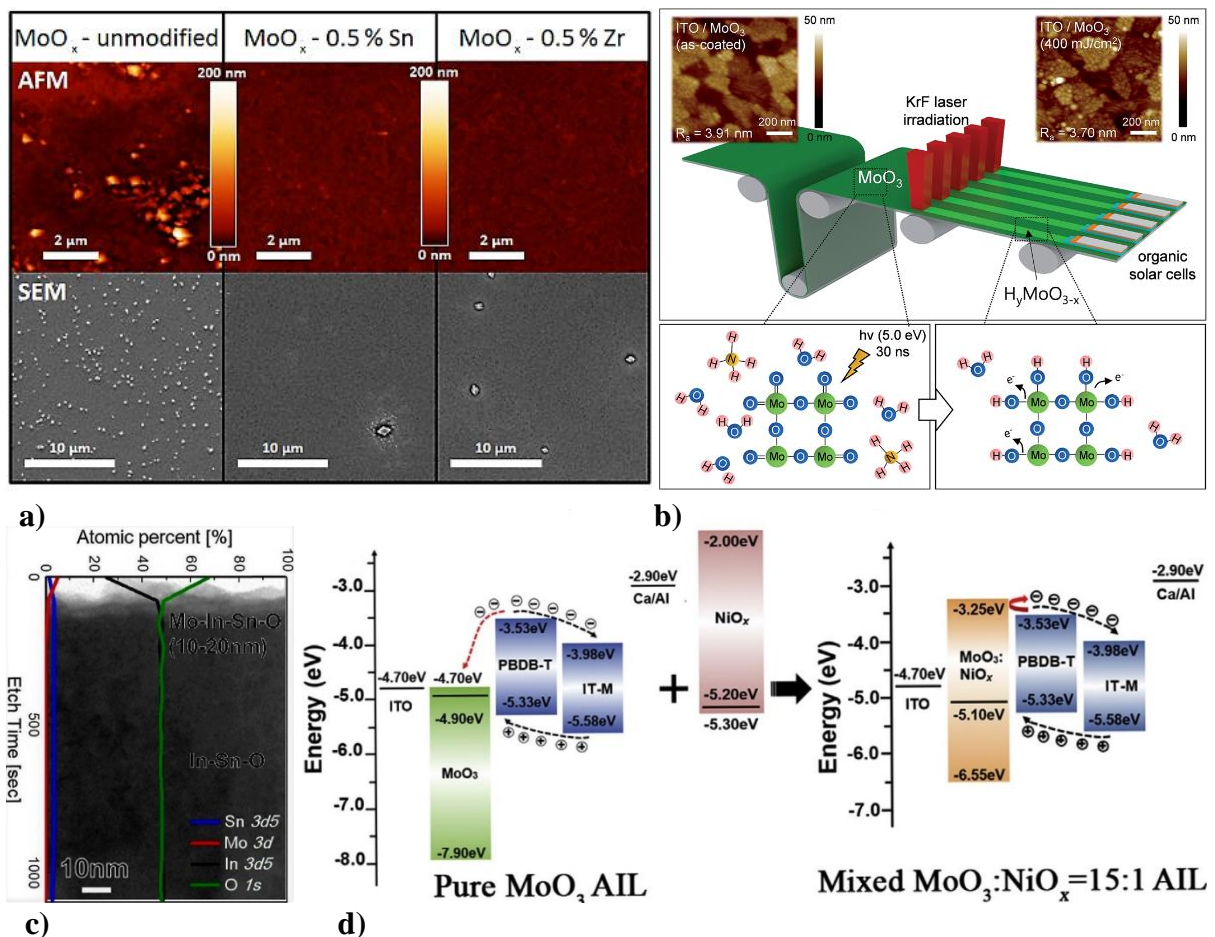


Figure 4. (a) Atomic force microscope (AFM) and scanning electron microscopy (SEM) images of unmodified and modified MoO_x HEL [114]. (b) Scheme of laser-assisted synthesis of H_yMoO_{3-x}. Reproduced from ref. [128] with permission from the Royal Society of Chemistry. (c) XPS depth profile of MGI electrode. Reproduced with permission from ref. [125]. Copyright 2016, Elsevier. (d) Energy levels of MoO₃ doped with NiO_x layer. Reproduced with permission from ref. [115]. Copyright 2019, Elsevier.

2.1.1.2 Tungsten Oxide

Tungsten oxide is an *n*-type material with a work function ranging from 4.7 to 6.4 eV depending on the film preparations^{129–132}. Tungsten oxide is a hole extracting layer that can work efficiently in conventional and inverted OSCs using vacuum as solution processing method^{69,133}. WO_x is an amorphous structure that: (i) forms smooth surface morphologies, (ii) increases the charge mobility in the active layer, (iii) enhances the charge collection because V_{oc} depends linearly on the anodic work function when there is not ohmic contact at the anode/donor interface¹³⁴. Thus, the enhancement in solution processing WO_x-based OSCs is particularly focused on increased light absorption.

Lee *et al.* designed an Au@SiO₂-WO₃ nanocomposite (NC) which works as a photon antenna for high light absorption¹³⁵. The localized surface plasmon resonance (LSPR) effect of Ag nanoparticles (NPs) enhances the intensity of photon absorption in the P3HT:PC₆₁BM BHJ cell, resulting in increased J_{sc}. Moreover, high hole mobility of WO_x NPs boosted the device PCE up 1.6%. The surface morphology of the Au@SiO₂-WO₃ NC film was kept uniform due to the SiO₂ shell avoided the aggregation effect of the Au NPs. Instead of SiO₂, the aggregation effect can be avoided by controlling the concentration of Au NPs. Using 10 wt% of Au NPs, the Au-WO₃ NC HEL decreased the surface morphology's roughness, achieving a PCE of 60.37%¹³⁶.

Shen *et al.* enhanced the light absorption and the PCE of the OSC from the LSRP effect of structure-differentiated silver nano-dopants in solution-processed WO_x HEL¹³⁷. In Figure 5a,b, from the three silver nano-dopants: (i) naked Ag NPs (nAgp), (ii) SiO₂-covered Ag NPs (SiAgp), and (iii) naked Ag nanoplates (nAgPI), the triangular nAgPI reached the higher efficiency of 4.6% while spherical nAgp the lowest. The spherical nAgp surface decreased the PCE because its surface can directly contact the donor/acceptor material of the active layer, resulting in excitons quenching; thus weak LSRP effects, see Figure 5c.

The layered structure of the hydrated phase of WO₃ allowed it to serve as a stable and efficient hole transport material¹³⁸. Remya *et al.* performed a study between dehydrated and di-hydrated WO₃ films as HEL in the inverted P3HT:PC₆₁BM and PTB7:PC₇₁BM cells¹³⁹. The hydrated phase of WO₃ enabled a suitable energy level alignment with the active layer by tuning the water coordination, resulting in a higher PCE of 5.1% and 7.8%, respectively.

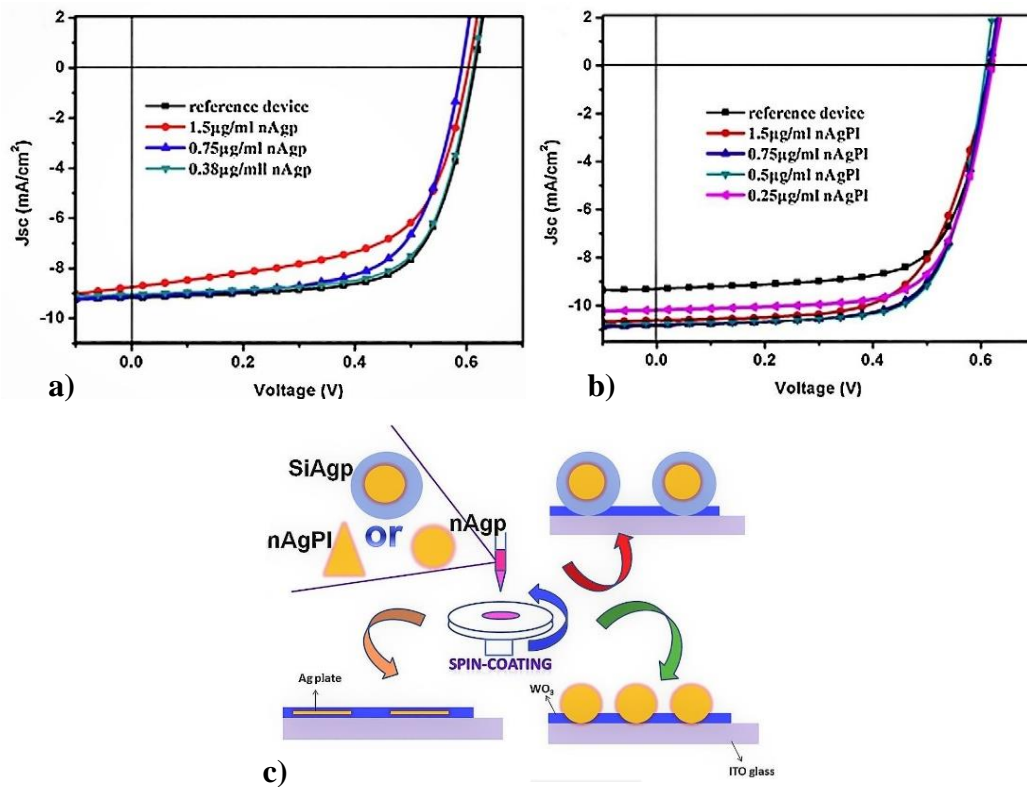


Figure 5. J-V curves with various concentrations of (a) nAgp, (b) nAgPI; (c) Structure-differentiated silver nanoparticles-doped WO₃ layers. Reproduced with permission from ref. [137]. Copyright 2016, Elsevier.

2.1.1.3 Vanadium Oxide

V₂O₅ is an adequate hole transporting and electron-blocking layer, resulting in improved efficiency and stability¹⁴⁰. V₂O₅ acts as a protecting layer, avoiding the surface reactions or the moisture from the working conditions¹⁴¹. The electronic structure of V₂O₅ corresponds to an *n*-type material with deep electronic states and WF ranging from 4.7 eV to 7.0 eV, depending on the processing method^{68,142}.

Xu *et al.* reported a low-temperature solution-processed V₂O₅ by dissolving the V₂O₅ powder into water solvent at room temperature¹⁴³. The device structure of ITO/V₂O₅/PTB7:PC₇₀BM/LiF/Al showed a PCE of 8.05% compared to PEDOT:PSS of 7.46%. V₂O₅ served as an optical spacer to increase light absorption, leading to a higher photocurrent. V₂O₅ powder can also be treated directly from the melting-quenching sol-gel method to obtain an easy tunable V₂O₅·*n*H₂O HEL¹⁴⁴. The energy positioning of the V₂O₅·*n*H₂O HEL (with *n* = 1) was closer to PEDOT:PSS⁵¹, allowing an ohmic contact with the novel conjugated polymer donor (PBDS_e-DT2PyT) and the acceptor of P₇₁BM; thus, a large V_{oc} and a PCE of 5.87% was obtained. The layered and hydrated phase of V₂O₅ is an accessible tunable charge transport

material by modifying the internal water coordination. Although $V_2O_5 \cdot H_2O$ -based HELs exhibiting better performance than PEDOT:PSS, the melting–quenching sol-gel method is expensive by the high temperature melting of V_2O_5 (~ 800 °C).

Cong *et al.* applied a green method to prepare vanadium oxide hydrate layers ($VO_x \cdot nH_2O$) to enhance the PCE in organic PTB7-Th:PC₇₁BM and P3HT:PC₆₁BM based polymer solar cells up to 8.11% and 3.24%¹⁴⁵. The combined H_2O_2 and ultraviolet ozone (UVO) in-situ treatments allowed for a smooth surface and improved wettability with the presence of dangling bonds on the surface HEL to enhance interfacial contact. The presence of V^{4+} in the composition analysis of $VO_x \cdot nH_2O$ accounted small amount of oxygen vacancies, causing *n*-type doping, which is essential to hole transport by extracting electrons through its conduction band¹⁴⁶. Vishnumurthy *et al.* reported that V_2O_5 HEL optimized the efficiency of thienothiophene-diketopyrrolopyrrole-based OSCs up 1.02%¹⁴⁷.

Remya *et al.* prepared an efficient hole transport/electron blocking hydrated vanadium oxide (HVO) from V_2O_5 powder with hydrogen peroxide¹⁴⁸. In the P3HT:PC₆₁BM and PBDTT-FTTE:PC₇₁BM BHJ cells, HVO HEL performance was superior to PEDOT:PSS, obtaining 56% enhancement (7.12–11.14%) in the PCE for the PBDTT-FTTE:PC₇₁BM-based inverted OSC with a lower degradation of 1.4% over 20 weeks.

In addition to the V_2O_5 powder, V_2O_5 HEL can be prepared by other precursors. Xu *et al.* reported an ammonium metavanadate ammoniacal water solution for processing VO_x HELs in PTB7:PC₇₁BM BHJ cells with a PCE of 7.7%¹⁴⁹. This HEL showed a work function of 5.3 eV and high conductivity by air annealing treatment at 210 °C for 5 min. The thermal treatment smoothed the surface film to reduce the leakage current, obtaining a higher J_{sc} . Although the stability was better than PEDOT:PSS with a remaining 83% efficiency after four days, it was still low compared to other inorganic HELs. Shafeeq *et al.* reported the formation of uniform and crystalline V_2O_5 nanorods by thermal decomposition of ammonium metavanadate NH_4VO_3 to enhance surface morphology and efficiency of OSCs¹⁵⁰.

Alsulami *et al.* obtained a stable V_2O_x HEL by using vanadium (V) oxytriisopropoxide as the precursor, which converted into V_2O_x by hydrolysis in air¹⁵¹. The PCE of the V_2O_x HEL was insensitive to thermal annealing at 100 °C and 200 °C because its optical and electronic properties were comparable to the vacuum-deposited V_2O_5 . Besides, the highly tunable V_2O_5 thin films prepared by this solution processing method help optoelectronic applications,

especially in inverted OSCs, by the higher stability under air conditions as reported by Zafar *et al.*¹⁵².

To optimize the interface properties and OSC performance, VO_x nanoparticle (NP) can efficiently be mixed with PEDOT:PSS solution, resulting in a stable VO_x:PEDOT:PSS HEL by the uniform molecular distribution of VO_x with PEDOT:PSS as reported Teng *et al.*¹⁵³. It achieved a PCE of 10.2% compared to PEDOT:PSS of 5.27% when VO_x:PEDOT:PSS was used as HEL in the TPD-3F:IT-4F cell. The V₂O₅ nanoparticles can fill the pinholes in PEDOT:PSS improving the conductivity and morphology of the composite HEL to increase the photocurrent and efficiency, as shown in PTB7-Th:PC₇₁BM-based OSCs (Figure 6a)¹⁵⁴. Xia *et al.* reported a nanoparticulate compact V₂O₅ film as HEL using a facile metal-organic decomposition method to replace the traditional HEL¹⁵⁵. By adding polyethylene glycol (PEG) as an additive in the precursor, an uniform and compact film of V₂O₅ served as HEL in the PTB7:PC70BM, improving the interface contact, J_{sc}, and the FF.

Compared to the spin coating, the spray coating of V₂O₅ HEL has allowed the large-scale production of flexible OSCs in a roll coater¹⁵⁶. Using a precursor solution of vanadium oxytriisopropoxide (VTIP) diluted in ethanol (1:100), V₂O₅ HEL exhibited improved electrical properties. The mechanical stress on V₂O₅ HEL was mitigated by introducing a PEDOT:PSS binding-interfacial layer between V₂O₅ HEL and the Ag electrode in the inverted P3HT:PC₆₀BM and PBDTTTz-4:PC₆₀BM BHJ cells. Arbab & Mola also explored electrochemical deposition that resulted in 80% enhancement in PCE (2.43%) compared with PEDOT:PSS-based OSCs¹⁵⁷.

Kavuri *et al.* reported electrospray deposition (ESD) for V₂O₅ HEL in the PTB7:PC₇₁BM OSC with a PCE of 7.61%¹⁵⁸. Because the surface morphology, charge mobility, and interfacial contact were adjusted in function of the solvent evaporation rate (6.25 μL/min), see Figure 6b. Compared to the spin-coating, the ESD allowed more control in the deposition conditions and reduced the manufacturing costs, making cost-effective the commercialization of V₂O₅-based OSCs.

V₂O₅ HEL has also been effective in ITO-free polymer solar cells with an optimized precursor solution (VTIP) of 0.005%¹⁵⁹. The deposition of V₂O₅ HEL on PEDOT:PSS, as the anode, led to increase R_{sh} and conductivity with the active layer of P3HT:PC₆₁BM by the hydrophobic surface of V₂O₅, resulting in an uniform and compact HEL with a PCE of 3.33%. V₂O₅ is also

a potential material to increase the anode's work function, indium zinc oxide (IZO), exhibiting a higher PCE of 2.8% than that flexible OSCs with only IZO, as reported by Ko *et al.*¹⁶⁰.

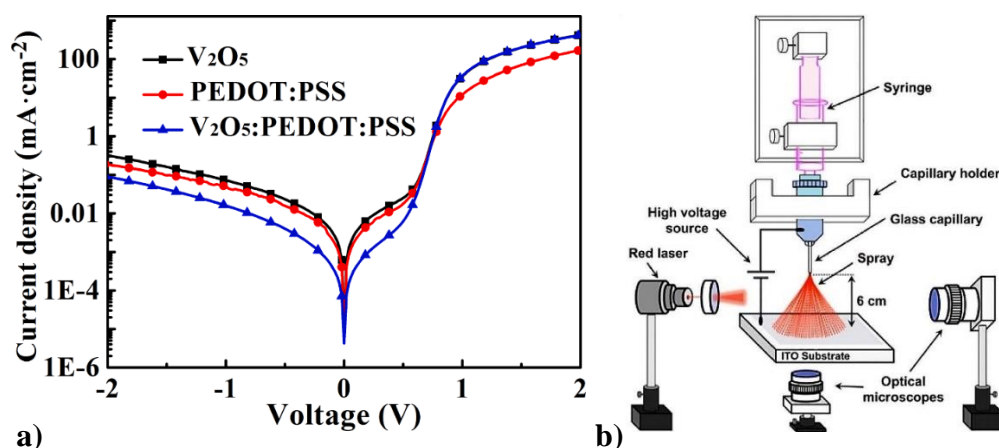


Figure 6. (a) J-V curve for V_2O_5 :PEDOT:PSS HELs in OSCs under the dark. Reproduced with permission from ref. [154]. Copyright 2020, Elsevier. (b) Electro spray setup. Reproduced with permission from ref. [158]. Copyright 2018, Elsevier.

2.1.1.4 Nickel Oxide

Non-stoichiometric NiO is a wide bandgap *p*-type semiconductor¹⁶¹. NiO is an efficient electron-blocking layer to the anode due to its conduction band minimum, 1.8 eV, which is above the LUMO of the organic donor P3HT (3.0 eV)⁷⁰. The ohmic contact between NiO and P3HT allows holes to freely transport from the active layer to the anode through Ni^{2+} vacancy-based hole-conducting anode band¹⁶².

Parthiban *et al.* demonstrated an enhancement in OSC performance with a NiO HEL deposited via spin coating¹⁶³. Using the precursor solution of nickel acetate and a simple post-annealing process (>300 °C) to reduce roughness, NiO HEL achieved a fill factor (FF) of 63.0% and a corresponding PCE of 4.45% was obtained in RP(BDT-PDBT):PC₇₀BM solar cell. Although, NiO-based HELs exhibiting better performance and stability than PEDOT:PSS, the high annealing temperature required to convert the nickel precursors into the NiO thin films is expensive and not compatible with flexible substrates. Chavhan *et al.* reported a low-temperature approach to manufacture NiO_x films from a nickel formate precursor solution via UV-ozone treatment at as low as room temperature¹⁶⁴. In terms of efficiency, the UV-ozone treatment results ideal for increasing the work function by creating hydroxides at the surface, avoiding high processing temperatures. A high PCE of 6.1% in NiO_x HEL treated with UV-ozone was related to NiO(OH) 's increased presence at the surface.

To date, the high surface roughness of FTO has limited its application in OSCs; however, the surface roughness can be decreased from 6.74 nm to 2.44 nm by fully covering it with an optimized NiO layer as reported by Kim¹⁶⁵. A polyethylene glycol (PEG) assisted sol-gel process altered c-NiO/FTO surface because it has a stabilizing effect on NiO NPs, so it allowed for the crystallization of a close-packed structure of NiO film (Figure 7). The further deposition of PEDOT:PSS led to the formation of a free-pinhole layer with an RMS roughness of 2.44 nm and selective hole transport, increasing the PCE from 5.68% to 7.93%.

Although organic devices based on NiO HEL have emerged successfully in the photo-electronic field, it is vital to focus research efforts for printing technologies for large-area roll-to-roll production. Printing technology usually results in thick NiO films, increasing the interfacial area between the active and HEL layers, shortening hole carriers' migration due to its short lifetime¹⁶⁶. Singh *et al.* obtained a thin film of NiO_x controlling substrate processing conditions and the inkjet printing¹⁶⁷. Optimal conditions of UVO pretreatment, drop spacing, and substrate temperature at 25 °C resulted in a PCE of 2.60% in the P3HT:PC₆₀BM cell with superior environmental stability. Huang *et al.* used copper (5.0 at.%) as a dopant to increase the electrical conductivity of NiO_x film, resulting in a reduction of R_s from 11.25 to 9.98 Ωcm²¹⁶⁸. The Cu-doped NiO_x (Cu:NiO_x) also improved the interface contact with the active layer and facilitated the charge transport, resulting in a higher PCE of 7.1% in the PCDTBT:PC₇₁BM cell.

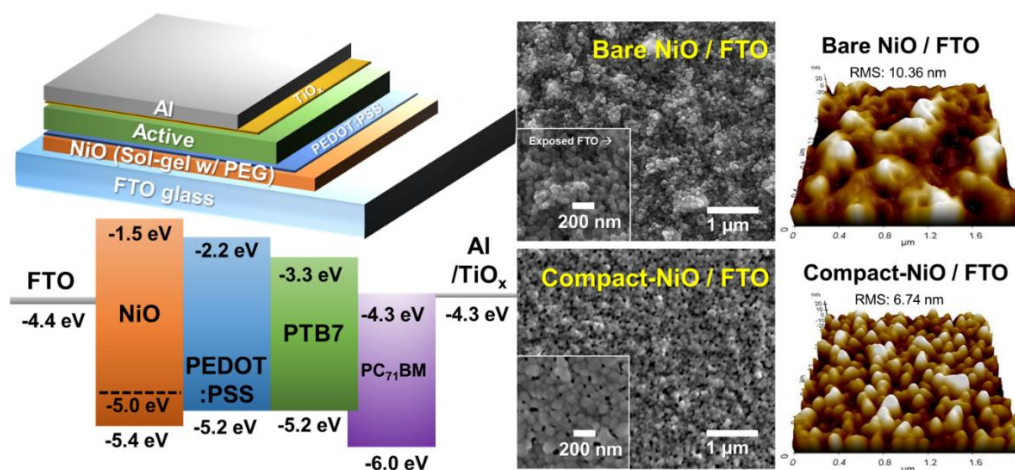


Figure 7. Atomic force microscope (AFM) images of bare nickel oxide on FTO (without PEG) and compact nickel oxide (c-NiO) on FTO (with PEG) [165].

2.1.1.5 Copper Oxide

CuO_x is a *p*-type semiconductor with narrow band gaps of CuO (1.3–2.0 eV) and Cu₂O (2.1–2.3 eV)^{169–172}. A HEL of CuO_x spin-coated on ITO decreased the interfacial barrier using a green solvent of copper acetylacetonate (Cu(C₅H₇O₂)₂), improving cell efficiency of PTB7:PC71BM cell to 8.68%¹⁷³. After H₂O₂ and UVO treatment, CuO_x HELs increased the work function to 5.45 eV, forming an excellent ohmic contact, and the V_{oc} increased to 0.74 V. Furthermore, the oxidation of CuO_x by UVO treatment enhanced the interfacial contact and the light absorption in the visible range obtaining high transmittance of 88%, low R_s of 2 Ωcm², and higher hole transport to the anode. The OSCs' initial performance (8.68%) dropped down to 47% over 50 hours of storage in the air.

2.1.1.6 Copper Chromium Oxide

The *p*-type CuCrO₂ is a semiconductor that belongs to the delafossite compounds¹⁷⁴. CuCrO₂ HELs are of great interest in optoelectronic applications due to the high transparency, large hole diffusion coefficient, high work function, and ionization energy, which are essential in the manufacture of OSCs^{175–177}.

New alternative techniques to produce efficient and cost-effective CuCrO₂ HELs for the roll-to-roll manufacturing are developing, such as microwave assisted-heating to produce CuCrO₂ nanocrystals with efficient PCE of 4.9%¹⁷⁸, or the combustion synthesis to produce CuCrO₂ thin films by low-temperature processing at 180 °C with a PCE of 4.6%¹⁷⁹. Both methods are highly efficient and represent advances for lowering the fabrication's costs. Further, UV-ozone post-treatment or annealing increases the metallic copper oxidation to Cu⁺² to promote the electronic conduction by the hopping mechanism between Cu¹⁺ and Cu⁺² species. The higher oxidation state of Cu⁺² enhanced the electronic properties, exhibiting deeper ionization energy (IE) and Fermi energy (EF) (see Figure 8). The Cu doping favored the surface roughness reduction, resulting in an improved interfacial contact, and thus favored J_{sc}, FF, and PCE, as recorded in Table 1.

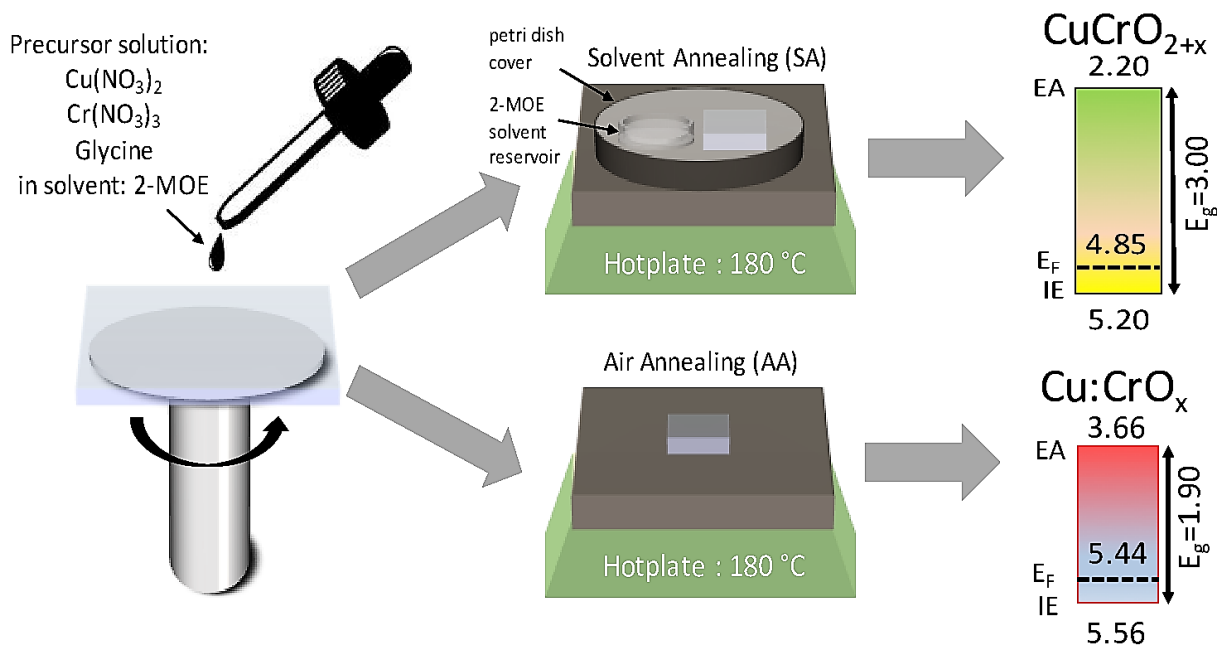


Figure 8. Schematic diagram of the combustion synthesis. Reprinted with permission from ref. [179]. Copyright 2018, American Chemical Society.

2.1.1.7 Indium Tin Oxide

Wahl *et al.* reported the first HEL based on ITO NPs in inverted organic solar cells¹⁸⁰. The addition of ethylenediamine into ITO NPs stabilized it to deposit uniform HELs on the underlying absorber layer. The deposition of the ITO NPs HELs by doctor blading allowed to control the thickness between 15 and 20 nm. Post-treatments of thermal annealing and plasma were beneficial for the film's electronic properties, achieving a PCE of 3%. However, plasma application needs to be gentle to avoid OSCs' detrimental performance. The doping method using high work function metals might be a good alternative over plasma treatments to develop high-quality films in organic solar cells.

2.1.1.8 Cobalt Oxide

The solubility of metal oxides in common solvents such as DMF or water is another main factor for its application in the roll-to-roll manufacturing of organic solar cells. Bhargav *et al.* reported the suitability of DMF soluble Co_3O_4 as HELs in PCDTBT:PC₇₁BM BHJ¹⁸¹. Co_3O_4 HELs showed transparency around 81% and a smooth surface, allowing for remarkable high FF of 49.1% and higher PCE (3.21%) compared to PEDOT: PSS-based OPVs.

2.1.2 Metal sulfides

2.1.2.1 Molybdenum disulfide

MoS₂ with a layered structure is a metal dichalcogenide (TMD) semiconductor that can display two phases under normal conditions: (i) the traditional trigonal prismatic H-MoS₂ phase and (ii) the distorted octahedral ZT-MoS₂ phase with hole mobilities of $3.8 \times 10^2 \text{ cm}^2 \text{V}^{-1} \text{s}^{-1}$ and $5.7 \times 10^4 \text{ cm}^2 \text{V}^{-1} \text{s}^{-1}$ ¹⁸². These particular electronic structures of MoS₂ have the characteristics to be proposed as a potential material for hole extraction in OSCs.

Instead of a vacuum or temperature-dependent process to prepare the traditional MoS₂ HEL, Barrera *et al.* prepared suspensions of MoS₂ via liquid exfoliation at room temperature¹⁸³. The high work function of MoS₂ resulted in enhanced charge mobility; however, the low transmittance of the film affected the J_{sc}, as recorded in Table 1. An effective way to address films' low transmittance is by using composites or hybrid layers with tunable transparency. Martinez-Rojas *et al.* reported a hybrid layer of MoS_x:MoO₃ with high transmittance on the FTO substrate¹⁸⁴. They obtained the hybrid layer using the pulsed electrochemical method. After 150 cycles of depositing MoS_x on the MoO₃, the percentage of transmitted light decreased significantly due to the agglomeration of MoS_x (Figure 9a). A hybrid layer with 100 cycles of deposition resulted in 10% higher PCE than the one obtained using MoO₃ or MoS_x HEL (see Table 1). MoS_x was an efficient electron blocking layer, while MoO₃ increased conductivity, resulting in enhanced hole-transporting properties.

The effectiveness of ultraviolet ozone (UVO) treatment to form homogeneous films and increase the work function was tested in a layer of MoS₂ quantum dots (QDs), showing a PCE of 2.62% and 8.7% for P3HT and PTB7-Th donor systems¹⁸⁵. The solar cell efficiency increased by 30 min UVO exposure, but more extended UVO treatment periods degraded the HEL, resulting in decreased PCEs (Figure 9b). The UVO-MoS₂ QDs showed compact and uniform layers with a lower surface roughness of 1.19 nm than UVO-MoS₂ nanosheets of 2.03 nm. The OSC achieved long-term durability due to the improved interfacial contact, showing 64% of its initial PCE after 47 days (Figure 9c).

Annealing treatments can also decrease the surface roughness and favor the optoelectronic properties of the film. At 300 °C, MoS_x flattened the surface morphology, enhancing the PCE up

to 7.5%, which was retained in 52% after two months¹⁸⁶. However, an annealing treatment is not as efficient as a UVO treatment in temperature-sensitive devices.

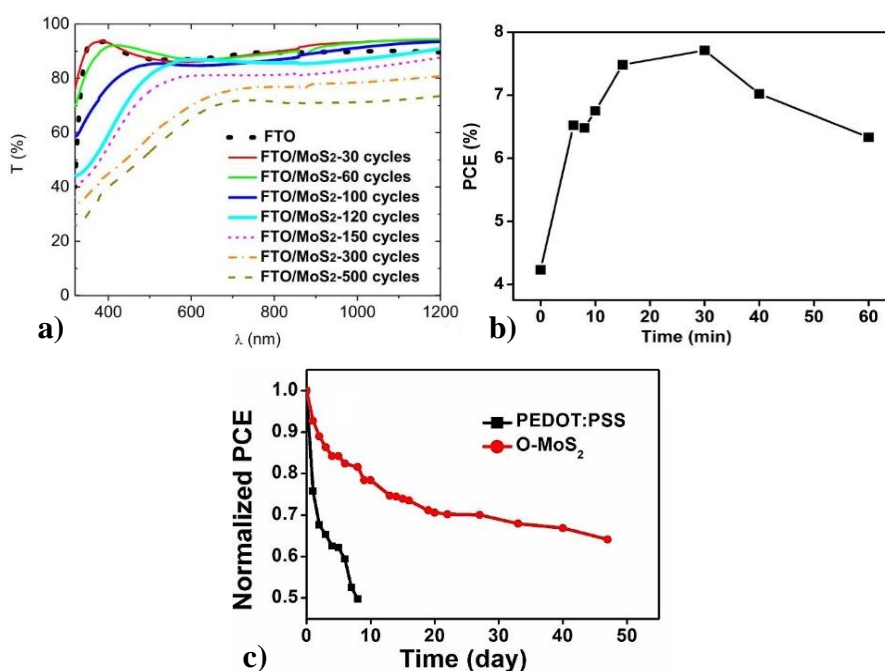


Figure 9. (a) Transmission spectra of FTO/MoS₂ with the number of scan cycles. Reproduced with permission from ref. [184]. Copyright 2017, Elsevier. (b) Dependence of PCE on UVO treatment; (c) Stability of devices using UVO-MoS₂ QDs than PEDOT:PSS HELs. Reproduced with permission from ref. [185]. Copyright 2016, American Chemical Society.

2.1.2.2 Tungsten disulfide

Adilbekova *et al.* used a liquid-phase exfoliation technique to manufacture WS₂ HEL using aqueous ammonia that does not require high-temperature post-treatments¹⁸⁷. Stabilizers or post-processing treatments were excluded from obtaining WS₂ nanosheets since stoichiometric quality, and structural properties were unchanged after performing the top-down method. Due to the *p*-type character of the 2D nanosheets, the HELs were selective to hole transport toward the anode, achieving a PCE of 15.6% in the PBDBT-2F:PC₇₁BM BHJ cell. Following the same line, Lin *et al.* fabricated uniform WS₂ layers on ITO¹⁸⁸. WS₂ flakes were larger in lateral size and thinner than MoS₂, covering the whole surface of ITO. The surface coverage was dependent on the shape and size of the selected material obtained by the exfoliation procedure and its interaction with the substrate. WS₂ HEL application in OSC in ternary BHJ systems (PBDB-T-2F:Y6:PC₇₁BM) increased PCE to 17%. Ram *et al.* demonstrated that the use of WS₂ as HEL increased the PCE of PBDB-T-2F:Y6:SF(BR)₄ ternary cells up 20.87%¹⁸⁹. The low

hygroscopic nature and low acidity of WS₂ reduced the contact resistance between the active layer and the ITO.

2.1.2.3 Nickel sulfide

Taking advantage of the dependence of the phase diagrams of NiS with the sulfur content, Hilal & Han synthesized the hexagonal phase of NiS as HEL in OSCs processed by the simple solvothermal method at room temperature¹⁹⁰. The surface morphology of NiS was smoothed by increasing the sulfur content to 2 g, forming a ball-shape flower-like NiS morphology with increased surface area (Figure 10). In addition to the enhancement in the hole transport, NiS stabilized the OSC to room temperature by the metallic nature of NiS. Hence, the P3HT:PCBM cell retained 26% of its initial efficiency value (2.28%) after 15 days.

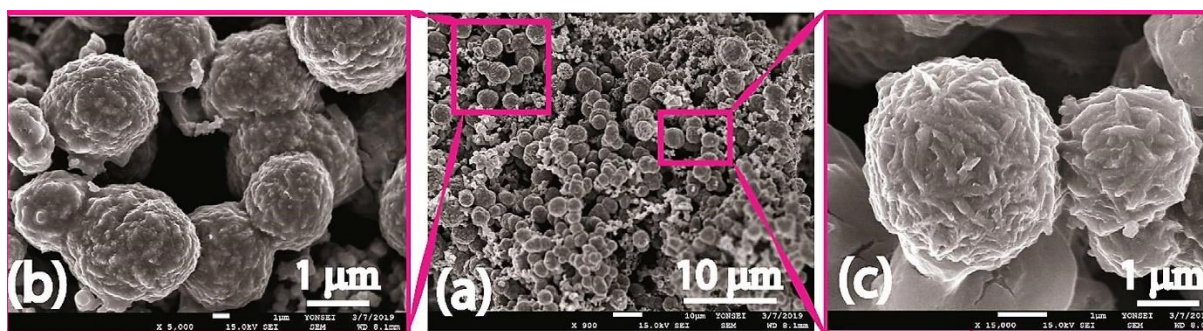


Figure 10. FE-SEM images of flower-shaped NiS (2.0) at magnifications of (a) 10 μm and (b, c) 1 μm. Reproduced with permission from ref. [190]. Copyright 2019, Elsevier.

2.1.2.4 Copper sulfide

An efficient organic solar cell was achieved by Bhargav *et al.* using an inorganic HEL made of CuS by a low-cost and efficient manufacturing process¹⁹¹. CuS thin film was deposited onto ITO by a solution process instead of vacuum deposition resulting in high transparency of 84%. Due to a decreased ohmic resistance, the device structure ITO/CuS/PTB7:P₇₁BM/Al reached a high PCE of 4.32% by the improved fill factor of 50.1%.

A new room-temperature method known as Successive Ionic Layer Adsorption and Reaction (SILAR) was reported by Jose *et al.* for the production of efficient *p*-type Zn-doped CuS HELs¹⁹². Due to the high conductivity and low light absorption in the visible region, a PCE of 1.87% was obtained with enhanced charge mobility of 1.5 cm²V⁻¹s⁻¹.

2.1.3 Miscellaneous

2.1.3.1 Copper(I) thiocyanate

The use of 2D materials like antimonene quantum dots (AMQS) in HELs has emerged in OSCs production due to the facile synthesis and unique properties¹⁹³. Wang *et al.* reached an enhanced PCE of 8.8% by the surface passivation of copper(I) thiocyanate (CuSCN) HEL with antimonene quantum sheets (AMQSs)¹⁹⁴. The AMQSs smoothened the film surface of CuSCN, tuned the work function and raised the exciton generation rate from $8.79 \times 10^{27} \text{ m}^{-3}\text{S}^{-1}$ to $9.95 \times 10^{27} \text{ m}^{-3}\text{S}^{-1}$. Compared to PEDOT:PSS HELs, CuSCN/AMQSs HELs were very stable at room temperature, remaining 68% of the initial PCE over 1 month not only in fullerene systems such as PTB7-Th:PC₇₁BM, but also in non-fullerene systems.

The *p*-doping of CuSCN with C₆₀F₄₈, an electron acceptor, is an effective method to obtain highly conductive hole transporting layers for its application in OSC devices¹⁹⁵. Due to the added 0.5 mol% of C₆₀F₄₈ also acts as a nucleating agent, the CuSCN:C₆₀F₄₈ film was higher density than the pristine CuSCN surface with reduced surface roughness, leakage current (Figure 11a), and improved hole mobility of $0.18 \text{ cm}^2\text{V}^{-1}\text{s}^{-1}$ attributed to the percolation conduction mechanism resulting in a PCE of 6.6% in the PCDTBT:PC₇₀BM.

Dong *et al.* reported a bilayer structure of copper(I) thiocyanate (CuSCN) and poly[(9,9-dioctylfluorenyl-2,7-diyl)-alt-(4,4'-(N-(4-butylphenyl)))] (TFB) as HEL in fullerene PTB7-Th:PC₇₁BM and non-fullerene PM6:Y6 systems¹⁹⁶. TFB enabled the fine-tuning of the work function of CuSCN to overcome the recombination loss and the lower exciton dissociation, achieving >14% efficiency than with CuSCN HEL. Wang *et al.* achieved a PCE of 15.28% in a cell based on the non-fullerene PM6:Y6 blend by doping CuSCN film with 1% of TFB (Figure 11b)¹⁹⁷. Worakajit *et al.* increased the hole mobility in CuSCN from 0.01 to $0.05 \text{ cm}^2\text{V}^{-1}\text{s}^{-1}$ by passivating surface morphology and the crystallinity with diethyl sulfide (DES) molecules and acetone as antisolvent treatment¹⁹⁸.

2.1.3.2 Copper Cadmium Tin Sulfide

At room temperature, Suresh Kumar *et al.* succeeded in fabricating Cu₂CdSnS₄ (CCTS) HELs over ITO substrates deposited by spin coating¹⁹⁹. A favorable PCE of 3.63% in the P3HT:PC₇₁BM blend was achieved by controlling the distribution particle size because the bandgap decreases with an increase in the size of CCTS and layer thickness. Minimum surface

roughness of 11.07 nm was found after three layers of CCTS thin films were coated, implying the thin film's compactness, efficient hole transport, and stability in environmental conditions.

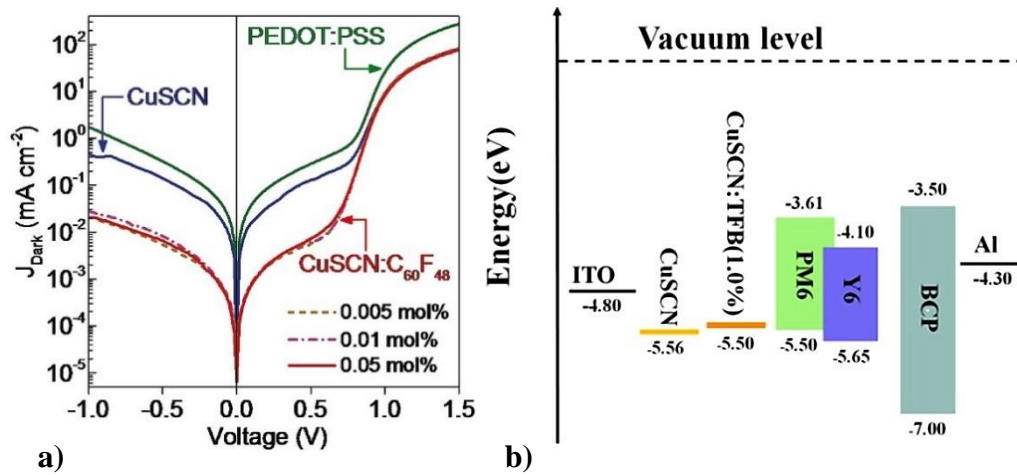


Figure 11. (a) J-V curves of CuSCN:C₆₀F₄₈ under dark conditions. Reproduced with permission from ref. [195]. Copyright 2018, John Wiley and Sons. (b) Energy level alignment of CuSCN:TFB (1.0%). Reproduced with permission from ref. [197]. Copyright 2020, American Chemical Society.

Table 1. Performance parameters of OSCs with inorganic films as hole transporting layers.

<i>Anode Configuration</i>	<i>Deposition Technique</i>	<i>Architecture of the active layer</i>	V_{oc} (V)	$J_{sc}(mAcm^{-2})$	FF (%)	PCE (%)	<i>Ref.</i>
ITO/s-MoO ₃	spin coating	PBDB-T-2F:Y6	0.84	27.53	73.10	17.00	110
ITO/MoO ₃ :PEDOT:PSS	spray casting	PBDB-T-2F:IT-4F	0.86	21.71	70.00	13.19	97
ITO/MoO ₃	spin coating	PBDB-T:PC71BM	0.88	17.48	0.71	10.86	104
MoO ₃ :NiO _x	spin coating	PBDB-T:IT-M	0.94	17.26	66.63	10.81	115
e-MoO _x /Ag	spin coating	PTB7-Th:PC71BM	0.79	18.70	69.20	10.42	101
MoO ₃ (8)/AgAl(3)/MoO ₃ (1) /AgAl	thermal evaporation	PTB7-Th:PC71BM	0.78	19.60	61.90	9.79	102
CuBr-MoO ₃ /Ag	thermal evaporation	PTB7:PC71BM	0.75	19.65	65.20	9.56	117
MoO _x NPs /Ag	spin coating	PTB7- Th:PC 71 BM	0.79	18.05	65.20	9.50	101
ITO/MoO ₃	spin coating	PBDB-T:ITIC	0.91	15.19	66.59	9.17	109
ITO/s-MoO ₃	spin coating	PTB7-Th:PC71BM	0.79	16.69	67.10	8.90	110
MoO ₃ /Ag	thermal evaporation	PTB7-Th:PC70BM	0.81	15.90	67.80	8.67	100
ITO/p-MoO ₃	spin coating	PTB7:PC71BM	0.73	17.02	68.10	8.46	106
ITO/CTAB-MoO ₃	spin coating	PTB7:PC71BM	0.72	16.88	68.10	8.34	118
ITO/ (MoO ₃ /AuNPs)/MoO ₃)	spin coating	PTB7:PC70BM	0.73	14.40	73.00	7.68	122
ITO/sMoO	spin coating	PV10:PC70BM	0.73	13.57	72.55	7.19	103
ITO/MoO _x	thermal evaporation	PTB7:PC71BM	0.67	14.00	67.00	6.57	105

ITO/ H _y MoO _{3-x}	spin coating	PTB7:PC70BM	0.77	13.90	61.20	6.55	128
ITO/CTAB-MoO ₃	spin coating	P3HT:ICBA	0.82	10.40	67.40	5.80	118
ITO/MoO _x	thermal evaporation	PTB7-Th:PC71BM	0.74	14.50	44.80	5.52	105
FTO/s-MoO ₃	spin coating	P3HT:ICBA	0.82	11.50	58.00	5.40	108
FTO/MoO _x	spin coating	P3HT:PC71BM	0.65	12.72	0.61	5.00	107
MoO ₃ NPs/Pedot:Pss/Ag	spin coating	P3HT:PCBM	0.57	12.74	0.57	4.19	98
ITO/p-MoO ₃	spin coating	P3HT:PC71BM	0.59	10.70	63.70	4.02	106
ITO/MoO _x	magnetron sputtering	P3HT:PCBM	0.64	12.00	50.00	3.84	126
ITO/MoO ₃	spin coating	P3HT:PC70BM	0.61	9.27	66.70	3.77	91
ITO/MoO ₃	spin coating	PCDTBT:PC70BM	0.79	9.32	49.00	3.62	114
ITO/CuI/MoO ₃	spin coating	P3HT:PCBM	0.66	9.57	0.56	3.54	116
MoO ₃ Array /Ag	spray casting	P3HT:PC61BM	0.59	9.61	59.20	3.40	96
ITO/MoO ₃	RF/DC graded sputtering	P3HT:PCBM	0.60	8.93	57.87	3.11	125
MoO ₃ /LiF/MoO ₃ /Ag/MoO ₃	spin coating	P3HT:PCBM	0.57	7.98	61.00	2.77	124
ITO/MoO ₃	electric field-spray casting	P3HT:PCBM	0.57	10.00	47.40	2.71	127
ITO/MoO _x	spin coating	P3HT:PC60BM	0.49	7.84	60.00	2.31	200
ITO/MoO _x	thermal evaporation	PCPDTBT:PC71BM	0.61	8.95	41.10	2.24	105
ITO/MoO _x	spin coating	P3HT:PCBM	0.60	6.93	51.90	2.16	113

α -MoO ₃ /Ag	spin coating	P3HT:PC60BM	0.52	7.39	40.32	1.55	95
ITO/WO _x :PEDOT:PSS	spin coating	PBDB-TF:IT-4F	0.87	20.65	80.39	14.37	138
ITO/PCM4	blade-coating	PBDB-T-2F:Y6	0.83	16.06	68.28	14.30	119
WO _x nanosheets/Ag	spin coating	PTB7: PC71BM	0.81	16.42	58.19	7.76	139
ITO/nAgPI-doped WO ₃	spin coating	P3HT:PCBM	0.61	10.80	71.00	4.60	137
ITO/Au-WO ₃ NCs	spin coating	P3HT:PC61BM	0.54	5.33	0.61	1.70	136
ITO/Au-SiO ₂ -WO ₃ NC	spin coating	P3HT:PC61BM	0.61	4.72	54.00	1.58	135
HVO/Ag	spin coating	PBDTT-FTTE:PC71BM	0.82	22.51	60.19	11.14	148
VO _x :PEDOT:PSS/Ag	spin coating	TPD-3F:IT-4F	0.87	16.80	69.10	10.10	153
ITO/V ₂ O ₅ :PEDOT:PSS	spin coating	PTB7-Th:PC71BM	0.80	16.83	70.14	9.44	154
ITO/VO _x ·nH ₂ O	spin coating	PTB7-th:PC71BM	0.78	15.76	64.62	8.11	145
ITO/V ₂ O ₅	spin coating	PTB7:PC70BM	0.71	17.35	65.00	8.05	143
ITO/NP-V ₂ O ₅	spin coating	PTB7:PC70BM	0.72	15.81	69.01	7.89	155
ITO/s-VO _x	spin coating	PTB7:PC71BM	0.73	15.79	66.82	7.70	149
ITO/ESD-VO _x	spray casting	PTB7:PC71BM	0.74	15.30	0.67	7.61	158
ITO/s-V ₂ O _x	spin coating	PFDT2BT-8:PC70BM	0.87	10.20	67.10	6.30	151
ITO/V ₂ O ₅ ·H ₂ O	spin coating	PBDSe- DT2PyT:PC71BM	0.72	13.96	59.00	5.87	144
V ₂ O ₅ /Ag	spin coating	P3HT: PCBM	0.61	10.68	59.83	3.92	152
PEDOT:PSS/ V ₂ O ₅	spin coating	P3HT:PCBM	0.58	9.18	62.17	3.33	159

V ₂ O ₅ /PEDOT:PSS/Ag	slot die coating	PBDTTTz-4:PC60BM	0.81	7.64	52.93	3.28	156
ITO/VO _x ·nH ₂ O	spin coating	P3HT:PC61BM	0.78	15.76	64.62	3.24	145
PET/VGIZO/PEDOT:PSS	spin coating	P3HT:PC61BM	0.57	8.10	59.48	2.75	160
ITO/ V ₂ O ₅	electrochemical deposition	P3HT:PCBM	0.55	9.95	44.30	2.40	157
V ₂ O ₅ /PEDOT:PSS/Ag	slot die coating	P3HT: PC60BM	0.53	6.98	53.96	1.98	156
ITO/ V ₂ O ₅	thermal evaporation	DPPTTh:PC61BM	0.65	23.70	66.30	1.02	147
FTO/Cu:NiO _x	spin coating	PCDTBT:PC71BM	0.89	12.40	63.85	7.05	168
FTO/c-NiO	spin coating	PTB7:PC71BM	0.72	14.28	66.98	6.91	165
ITO/NiO _x	spin coating	TQ1:PC70BM	0.87	10.30	71.30	6.39	164
ITO/NiO _x	spin coating	RP(BDT- PDBT):PC70BM	0.71	9.85	63.00	4.46	163
ITO/NiO	inkjet printing	P3HT:PC60BM	0.60	8.57	50.10	2.59	167
ITO/CuO _x	spin coating	PTB7:PC71BM	0.74	16.44	71.00	8.68	173
ITO/CuCrO ₂	microwave-assisted	PCDTBT:PC71BM	0.87	9.31	0.60	4.86	178
ITO/CuCrO ₂	microwave-assisted	P3HT:PCBM	0.55	8.96	0.65	3.20	178
ITO/Cu:CrO _x	spin coating	PCDTBT:PC71BM	0.90	8.99	60.00	4.87	179
ITO NPs/Ag	doctor-bladed	P3HT:PC60BM	0.56	8.40	58.20	3.00	180
ITO/Co ₃ O ₄	spin coated	PCDTBT:PC71BM	0.68	11.90	49.10	3.21	181
ITO/MoS ₂	spin coating	PBDB-T-2F:Y6:PC71BM	0.81	25.30	71.00	14.90	187

ITO/O-MoS ₂ QDs	spin coating	PTB7-Th: PC71BM	0.79	16.90	65.00	8.66	185
ITO/MoS _x	spin coating	PTB7-Th: PC71BM	0.77	18.16	53.56	7.50	186
MoS ₂ /Ag	spray coating	P3HT:PCBM	0.50	6.18	64.50	2.00	183
FTO/MoS ₂ :MoO ₃	pulsed electrochemical deposition	CuPC:PC60BM	0.47	6.14	51.00	1.47	184
ITO/WS ₂	spin coating	PBDB-T-2F:Y6:SF(BR) ₄	0.89	29.31	80.00	20.87	189
ITO/WS ₂	spin coating	PBDB-T-2F: Y6: PC71BM	0.84	26.00	78.00	17.00	188
ITO/WS ₂	spin coating	PBDB-T-2F:Y6:PC71BM	0.83	26.00	0.72	15.60	187
ITO/NiS	spin coating	P3HT:PCBM	0.47	10.12	0.47	2.28	190
ITO/CuS	spin coating	PTB7:PC71BM	0.60	13.60	50.10	4.32	191
ITO/ Zn:CuS	SILAR coating	P3HT:PC71BM	0.45	11.50	36.00	1.87	192
ITO/CuSCN:TFB (1.0%)	spin coating	PM6:Y6	0.85	24.35	73.84	15.28	197
ITO/CuSCN:TFB	spin coating	PM6:Y6	0.85	24.45	72.69	15.10	196
ITO/CuSCN:AMQS	spin coating	PBDBT-2F:IT-4F	0.80	18.70	67.80	10.14	194
ITO/ CuSCN:AMQS	spin coating	PTB7-Th:PC71BM	0.79	17.10	65.20	8.80	194
ITO/CuSCN:TFB	spin coating	PTB7-Th:PC71BM	0.79	16.42	66.28	8.56	196
ITO/CuSCN:AMQSs	spin coating	PTB7-Th:ITIC	0.82	15.07	59.06	7.15	194
ITO/CuSCN:C ₆₀ F ₄₈	spin coating	PCDTBT:PC70BM	0.92	11.50	0.61	6.60	195
ITO/Cu ₂ CdSnS ₄	spin coating	P3HT:PCBM	0.62	8.99	65.18	3.63	199

2.2 Nanocarbon Hole Extracting Layers

2.2.1 Graphene Oxide

Nanocarbon materials like graphene have been applied in OSCs due to their unique electrical, optical, and structural properties²⁰¹. Due to the low water dispersibility caused by the nonpolar sp² hybridized carbon structure, the oxidized form of graphene, graphene oxide (GO), has also been used in OSCs by the high solubility in eco-friendly water solvents²⁰².

The hydroxyl groups and epoxy groups located in the basal plane of the graphene sheet and carboxylic acids at the edge limit the conductivity of GO for applying in OSCs²⁰³. In fact, an excess of 25% of oxygen atoms on the GO sheet's surface reduced its conductivity until it became an insulator material²⁰⁴. Thus, it is crucial to control the concentration and thickness of GO for suitable performance as HELs. Rafique *et al.* tested thickness and concentrations of spin-coated GO, selecting 1 mg/mL to form thin conductive films in bulk heterojunction organic solar cells with a PCE of 2.73%²⁰⁵.

The reduction process is another feasible way to increase the conductivity of GO layers. The reduction removes the excess of oxygen atoms from the GO surface and recovers the conjugated honeycomb structure²⁰⁶. Huang *et al.* succeeded in synthesizing eco-friendly reduced graphene oxide (rGO) by using a modified Hummer's method to produce GO and thermal treatment to reduce it²⁰⁷. A mild temperature of 280 °C was used to obtain rGO and enhance OSCs' conductivity based on P3HT:PC₇₁BM and PTB7:PC₇₁BM with a PCE of 3.39% and 7.62%, respectively.

The dispersibility must be controlled to ensure good coverage of the underlying substrate. Lee *et al.* mixed highly dispersible semiconducting fullerene surfactant with GO, obtaining water-dispersible and conductive films after reducing a PCE of 3.15%²⁰⁸. The conductivity increased from $5 \times 10^{-4} \text{ Scm}^{-1}$ for the pristine GO layer to $1 \times 10^{-2} \text{ Scm}^{-1}$ for fullerene-GO layer.

Chemical and physical methods involving the reduction of GO seek to tune the work function, improve electrical properties, reduce absorption, and increase hole mobility and charge collection capability. Kwon *et al.* obtained rGO by electron-beam irradiation with shorter processing times than reported gamma (γ)-rays²⁰⁹. Following the same line, Fakharian *et al.* applied YAG pulsed laser to produce rGO in formic acid for OPVs with a PCE of 4.02%²¹⁰.

They also highlighted solvent's role in manufacturing devices to achieve an rGO with superior physical and electrical features. Unlike the traditional chemical reduction methods, pulsed laser or electron-beam allowed the reduction of graphene over the in-situ formation of reducing species selectively. Dericiler *et al.* reported graphene nanosheets prepared from the electrochemical exfoliation of graphene powder followed by dispersion in DMF solvent²¹¹. They used the graphene nanosheets suspension as an additive to PEDOT:PSS HEL to enhance the stability and charge mobility in the P3HT:PC₆₀BM, achieving 66% enhancement in the PCE compared to the reference cell based on pure PEDOT:PSS.

The application of ultraviolet ozone (UVO) irradiation has shown excellent efficiency in reducing GO in large-scale OSCs manufacturing. Xia *et al.*²¹² and Rafique *et al.*²¹³ exposed GO to UVO treatment, obtaining optimized performance in P3HT:PC₇₁BM and PCDTBT:PC₇₁BM blend systems. UVO oxidizes the surface of GO and removes CO₂ molecules leaving a uniform, smoothed, and conductive film. Ultraviolet irradiation was controlled to remove only C-O bonds from the GO surface. UVO treated GO films allowed to exceed the value of FF and J_{sc} obtained from PEDOT: PSS, as recorded in Table 2.

Taking advantage of graphene's chemical structure, the functionalization is very promising for obtaining desirable properties in HELs, such as high hole mobility, charge collection, transparency, and stability, among others. Zhao *et al.* formed covalent bonds between graphene and sulfanilic acid using the C-N linker to fabricate highly stable P3HT:PC₇₁BM based OSCs with a PCE of 3.56%²¹⁴. The covalent functionalization increased the work function to enhance the interface's charge transport (Figure 12a). Ali *et al.* confirmed the potential for tuning the bandgap and electrical properties when reduced and sulfonated GO films were applied as HELs for a wide range of donor-acceptor systems²¹⁵.

Other approaches like non-covalent phosphorylation and fluorination have been remarkably effective in enhancing the charge collection and transport via inducing low ohmic contact^{216,217}. The presence of the phosphate ester or fluor in the surface of GO increased the work function of ITO/GO and tuned the HOMO level of the donor by the *p*-doping effect. Fluorinated GO (F₅-GO) was reported to work as an interlayer between ITO and PEDOT:PSS by Nicasio-Collazo *et al.*²¹⁸. This material improved hole transport resulting in a low R_s of 2 Ωcm² and a PCE of 7.67% for PTB7:PC₇₁BM based OSC.

Park *et al.* reported an orthogonal printable HEL by spray casting a highly stable dispersion of fluorine-functionalized reduced graphene oxide (FrGO)²¹⁹. By decreasing the sheet size to 0.3 μm , the PCE increased to 9.27 and 9.02% for PTB7-Th:EH-IDTBR and PTB7-Th:PC₇₁BM-based OSCs, which improvement was attributed to the hole transport efficiency, decreased leakage current, and higher conductivity than GO. Zhen *et al.* reported graphene-MoS₂ hybrid thin films via liquid-phase graphene exfoliation, improving the charge transportation as an interlayer to achieve a PCE 9.5%²²⁰. This interlayer increased the device stability by retaining 93% of the initial PCE after 1000 hours at room temperature. Shoyiga *et al.* reported reduced graphene oxide-anatase titania (RGOT) nanocomposites by hydrothermal synthesis²²¹. RGOT HEL is an efficient charge transport channel whose higher conductivity and exciton dissociation efficiency decreased the rates of electron-hole recombination (Figure 12b), resulting in a high J_{sc} , low R_s , and, thus, improved photovoltaic performance.

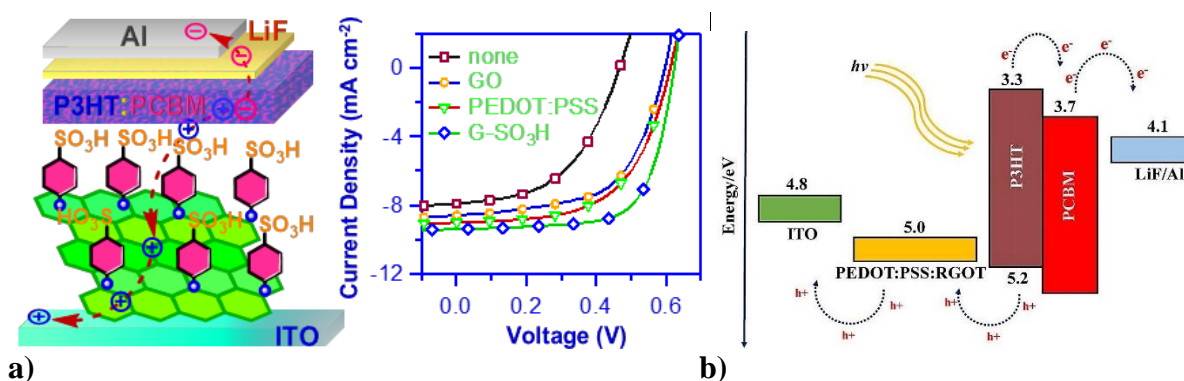


Figure 12. (a) J-V curve of the OSCs with G-SO₃H films as HEL. Reproduced with permission from ref. [214]. Copyright 2018, American Chemical Society. (b) Energy level diagram of RGOT modified hole extracting layer. Reproduced with permission from ref. [221]. Copyright 2020, John Wiley and Sons.

Lee *et al.* improved the performance of reduced graphene oxide (rGO) by chemical doping with tetrafluorotetracyanoquino-dimethane (F₄TCNQ)²²². The *p*-doping of rGO with F₄TCNQ increased the work function by 0.2 eV and the conductivity by inducing charge transfer between the F₄TCNQ and the graphene layer. F₄TCNQ enhanced the interchain interaction and crystallization of the P3HT film to improve the hole mobility from the active layer to the anode. Lee *et al.*²²³ and Sun *et al.*²²⁴ reported that GO modified with alkali chlorides, such as AuCl₃ or CuCl₂ dopants in a conventional architecture exhibited an average PCE of 3.77% and 7.68%, respectively. The AuCl₃ doped graphene increased the electrical conductivity ($\sim 2.0 \times 10^5 \text{ S m}^{-1}$) compared to the reported fullereneol-rGO layer ($1 \times 10^{-2} \text{ S cm}^{-1}$). GO:CuCl₂ layers formed a uniform and continuous film. Although the efficiency achieved by the dopants is even comparable to that of the control devices with PEDOT: PSS, the stability was superior.

Graphene-based derivatives (GBD) do not corrode the metal substrate as PEDOT:PSS, leading to the development of OSCs' efficient performance by controlling the properties and deposition conditions of GBD as reported by Capasso *et al.*²²⁵.

Sarkar *et al.* embed Au NPs into GO for increasing the light trapping in the active layer²²⁶. The exerted plasmonic effect and the plasmon-exciton interaction of NPs increased the light harvested by the active layer, resulting in enhanced J_{sc} and PCE, see Table 2. Besides, the enhanced conductivity of GO helped to reduce the leakage current, thereby improving the photogenerated current, R_s , and FF of the device.

A composite of 1wt.% of graphene nanosheet and water-dispersible polyaniline-poly(2-acrylamido-2-methyl-1-propanesulfonic acid) complex was used as HEL in organic solar cells²²⁷. The graphene nanostacks (GN) from the composite penetrated the bulk heterojunction of the OSC and facilitated the charge transport by forming additional pathways, see Figure 13. The electric field generated from the edges of the GN increased the exciton dissociation. As a result, the composite performance raised the PCE from 2.12% (PANI) to 2.92% (G-PANI) in the P3HT:PC₇₀BM cell. Abdulrazzaq *et al.* prepared acid-free PANI:graphene oxide nanocomposites as HEL to increase the stability and performance of P3HT:PC₆₀BM and PCDTBT:PC₇₀BM-based OSCs²²⁸. Aatif *et al.* also reported the surface morphology's planarization after applying GO/molybdenum composite, resulting in a PCE of 5.1% with the PCDTBT:PC₇₁BM based OSCs²²⁹.

Quasi-3D GO:NiO_x nanocomposites are potential *p*-type HELs in ITO/ZnO/PTB7-Th:PC₇₁BM/HEL/Ag architectures²³⁰. Using the solvothermal method, NiO_x NPs interacted with the low oxidized form of GO by hydrogen bonds to form the quasi 3-D arrangement (see Figure 13c). The high performance of these nanocomposites HELs is due to the enhanced vertical conductivity with low recombination rates and enhanced electron-blocking ability by the small conduction band of NiO_x NPs (1.55 eV) (Figure 13b). The metallic nature of NiO_x NPs improved the stability by remaining half of the initial PCE (12.3%) in environmental conditions.

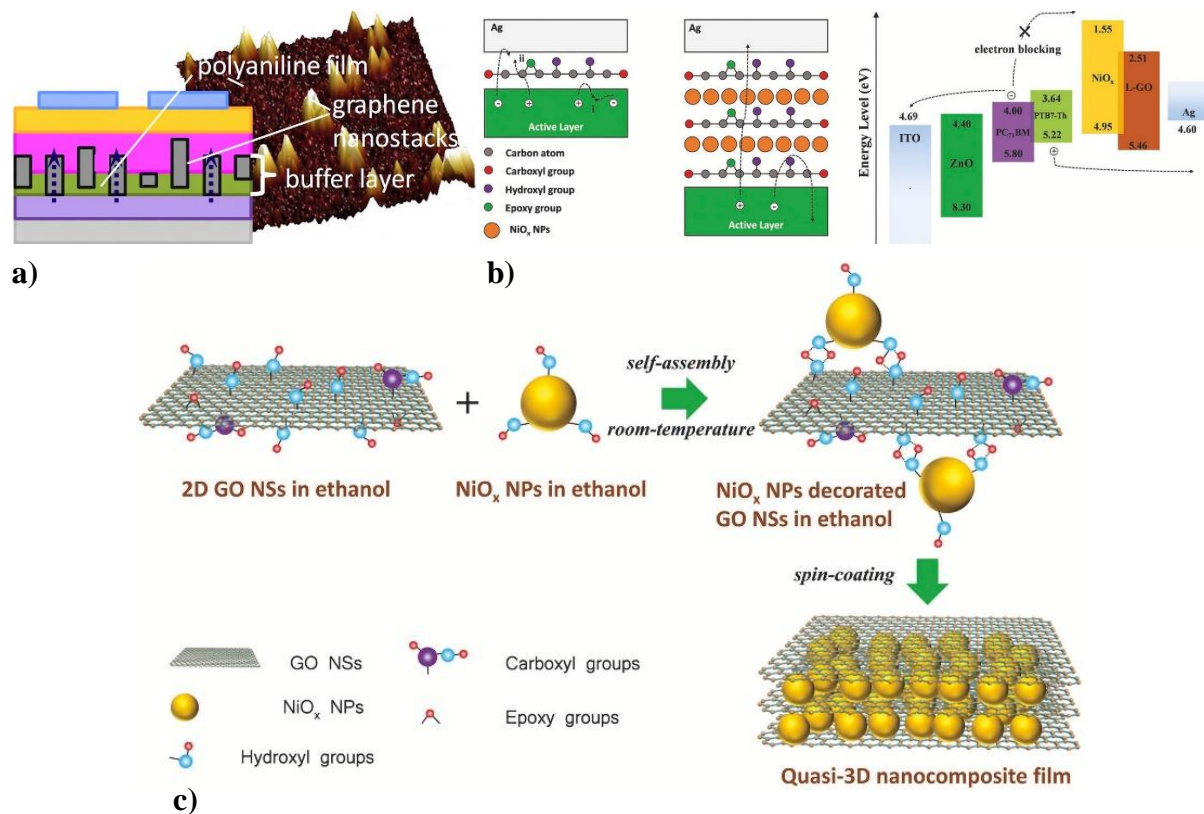


Figure 13. (a) Topography AFM-images of G/PANI-PAMPSA nanocomposite layer. Reproduced with permission from ref. [227]. Copyright 2018, Elsevier. (b) Hole extraction properties and dynamics at the interface; (c) Preparation at room temperature of self-assembled quasi-3D GO:NiO_x nanocomposite. Reproduced with permission from ref. [230]. Copyright 2018, John Wiley and Sons.

Dang *et al.* reported a solution-processed hybrid graphene-MoO₃ (G-MoO₃), via the hydrothermal method, to apply as HEL in organic solar cells²³¹. The G-MoO₃ exhibited high transparency in the visible region compared to the thermal evaporated MoO₃. Moreover, the low injection barrier (0.2 eV) and the higher hole mobility of G-MoO₃ ($4.16 \times 10^{-5} \text{ cm}^2 \text{V}^{-1} \text{s}^{-1}$) than MoO₃ ($1.25 \times 10^{-5} \text{ cm}^2 \text{V}^{-1} \text{s}^{-1}$) were beneficial to achieve a high PCE of 7.07 %. The reduced graphene oxide (rGO) and perylene derivative (3,4,9,10-perylenetetracarboxylic dianhydride (PTCDA) nanohybrid is a potential HEL for increasing the PBDTTT-CT:PC₇₁BM cell performance up 4.70%²³². The rGO:PTCDA nanohybrid HEL formed permanent dipoles by the PTCDA_rGO bond formation, increasing the hole extraction, electrical conductivity, and tuning the work function.

2.2.2 Graphene Quantum Dots

The production efficiency of graphene quantum dots (GQDs) in the photovoltaic field has been limited by the expensive manufacturing methods, materials availability, and the time-

consuming^{233,234}. However, the development of green and low-cost methods, such as the synthesis of GQDs from carbon fibers by acid treatment and chemical exfoliation or doping with nitrogen, has boosted its potential application in the large-area fabrication of OSCs^{234,235}. Hoang *et al.* succeeded in the green synthesis of GQDs from graphene using the microwave-assisted hydrothermal method for 10 min²³⁶. An enhancement of 44% in PCE was achieved by doping the active layer with 2 mg of GQDs. The GQDs filled the interstitial positions between P3HT and PC₆₀BM to increase the charge transport of holes and electrons and the photocurrent generation.

2.2.3 Carbon Nanotubes

Zhang *et al.* reported amino-functionalized multi-walled carbon nanotubes (a-MWNTs), via hydrothermal synthesis, as HELs in conventional OSCs with the configuration ITO/a-MWNTs/PCDTBT/PC₇₁BM/LiF/Al²³⁷. Compared to the carboxylic acids, the amino functionalization reduced the defects and the resistivity of a-MWNTs (Figure 14a). The a-MWNTs enhanced the device's charge mobility, collection, and performance to 6.9%.

2.2.4 Single-Walled Carbon Nanotubes

Single-walled carbon nanotubes (SWCNTs) are promising *p*-type transparent conductors owing to their superior hole mobility, conductivity, and facile tuning of the work function by doping method²³⁸. In Figure 14d, the highly-conductive composite of unzipped single-walled carbon nanotubes (u-SWNTs) and PEDOT:PSS was synthesized by a facile solution processing method as reported by Zhang *et al.*²³⁹. The hybrid PEDOT:PSS doped with u-SWNTs decreased the surface roughness, and oxygen-containing groups of u-SWNTs improved the compatibility between u-SWNTs and PEDOT:PSS to block electrons and increase the hole transport. Using 0.1 mgmL⁻¹ of u-SWNTs, the conductivity of the uSWNTs/PEDOT:PSS increased to 2.08 Scm⁻¹, and R_s was insensitive to the layer thickness, resulting in improved charge carriers transport through the gap of u-SWNTs (Figure 14c). Thus, PBDB-T-2F:IT-4F devices with u-SWNTs/PEDOT:PSS HELs exhibited an enhancement in the PCE from 13.72% to 14.60% (Figure 14b).

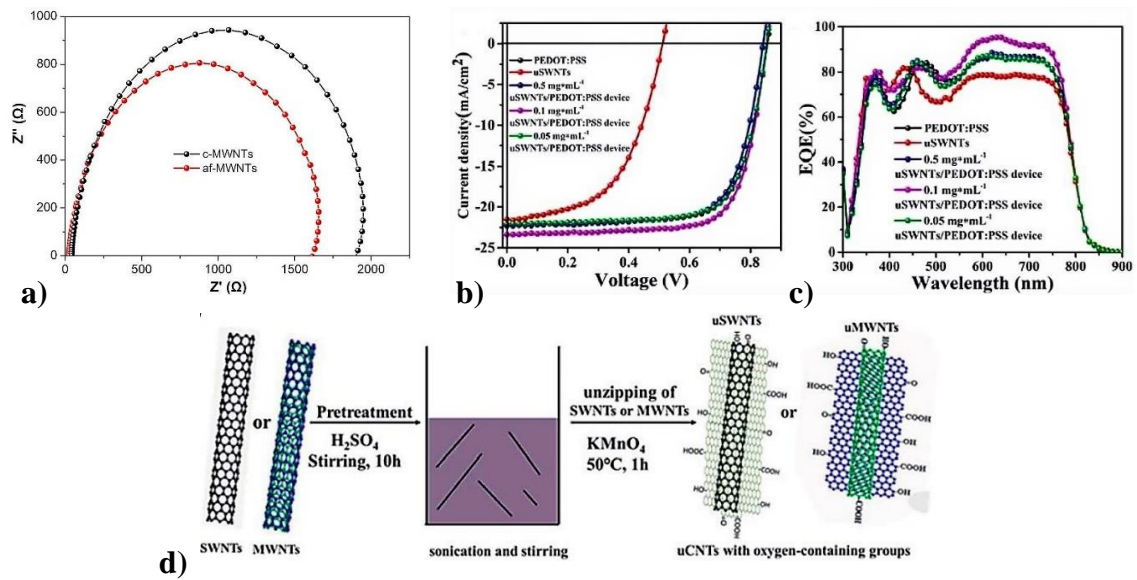


Figure 14. (a) Impedance spectra of OSCs with c-MWNTs and af-MWNTs HELs. Reproduced with permission from ref. [237]. Copyright 2019, Elsevier. (b) J-V curves of the OSCs with u-SWNTs HELs; (c) External quantum efficiency (EQE) of u-SWNTs, SWNTs, and PEDOT:PSS; (d) Schematic of u-SWNTs or u-MWNTs synthesis [239].

Table 2. Performance parameters of OSCs with carbon-based films as hole transporting layers.

<i>Anode Configuration</i>	<i>Deposition Technique</i>	<i>Architecture of the active layer</i>	V_{oc} (V)	$J_{sc}(mAcm^{-2})$	FF (%)	PCE (%)	<i>Ref.</i>
ITO/uSWNTs/PEDOT:PSS	spin coating	PBDB-T-2F:IT-4F	0.85	23.39	73.17	14.60	239
ITO/FrGO	spray casting	PM6:Y6 PSC.	0.77	24.64	69.60	13.26	219
L-GO:NiO /Ag	spin coating	PBDB-T:IT-M	0.91	17.81	71.00	12.13	230
G-MoS ₂ /Ag	spin coating	PTB7-Th:PC71BM	0.80	17.10	67.70	9.50	220
ITO/G-MoS ₂ /PEDOT:PSS	spin coating	PTB7-Th:PC71BM	0.77	17.20	72.00	9.40	220
ITO/FrGO	spray casting	PTB7-Th:EH-IDTBR	1.00	14.86	61.80	9.22	219
ITO/F-rGO	spin coating	PTB7-Th:PC71BM	0.79	16.89	64.80	8.60	217
ITO/P-GO	spin coating	PTB7:PC71BM	0.71	16.12	68.40	7.90	216
ITO/GO:CuCl ₂	spin coating	PTB7-Th:PC71BM	0.79	15.52	63.00	7.74	224
ITO/G-MoO ₃	spin coating	PCDTBT:PC71BM	0.86	12.83	63.67	7.07	231
af-MWNTs	spin coating	PCDTBT:PC71BM	0.87	12.65	63.50	6.97	237
ITO/GO:NPs	spin coating	PTB7:PC71BM	0.75	11.55	67.91	5.88	226
ITO/F ₅ -rGO	spin coating	PTB7:PC71BM	0.68	14.78	57.30	5.82	218
ITO/GBD	spin coating	PBDTTT-C-T:PC70BM	0.71	13.38	52.54	5.01	225
GO:MoO ₃	spin coating	PCDTBT:PC71BM	0.66	16.16	47.11	5.10	229
ITO/rGO_PTCDA	spin coating	PBDTTT-CT:PC71BM	0.76	11.61	53.00	4.70	232

ITO/GO	spin coating	P3HT:PCBM	0.61	10.94	63.00	4.18	212
ITO/GO	spin coating	PCDTBT:PC71BM	0.85	9.40	51.00	4.07	213
ITO/r-GO	drop casting	P3HT:PCBM	0.64	10.15	62.00	4.02	210
ITO/G_SO ₃ H	spin coating	P3HT:PC61BM	0.61	9.38	67.00	3.83	214
ITO/Au_DFGFs/ PEDOT:PSS	spin coating	P3HT:PCBM	0.55	12.33	53.00	3.77	223
ITO/GO	spin coating	P3HT:PC71BM	0.59	10.93	52.60	3.39	207
ITO/ERGO	spin coating	P3HT:PCBM	0.60	9.35	62.61	3.52	209
ITO/r-GO	spin coating	P3HT:PCBM	0.58	8.42	64.00	3.15	208
ITO/N_GQDs	spin coating	P3HT:PCBM	0.58	8.50	60.00	2.96	235
ITO/G_PANI_PAMPSA	spin coating	P3HT:PC70BM	0.60	11.10	44.00	2.92	227
S-RGO/Au	spin coating	P3HT:PC61BM	0.60	7.54	62.00	2.80	215
ITO/GO	spin coating	PCDTBT:PC71BM	0.80	8.14	42.00	2.73	205
ITO/PEDOT:PSS-GO	spin coating	P3HT:PCBM	0.58	8.30	52.00	2.27	211
ITO/DRGO/F ₄ TCNQ	spin coating	P3HT:PCBM	0.57	7.00	49.10	2.17	222
GQDs/Al	spin coating	P3HT:PCBM	0.54	6.31	42.00	1.43	236
ITO/PEDOT:PSS:RGOT	spin coating	P3HT:PCBM	0.51	6.56	27.67	0.93	221

CHAPTER 3: Conclusions and Recommendations

Conclusions

In summary, HELs are fundamental to assure the high performance and stability of OSCs. Inorganic and nanocarbon materials including MoO₃, WO₃, V₂O₅, NiO_x, CuO_x, CoO_x, CuCrO_x, CuSCN, MoS₂, WS₂, NiS, CuS and GO, QCDs, CNTs have shown great potential as HELs in conventional and inverted OSCs. These hole extracting materials can form an ohmic contact between the active and electrodes depending on their optical and electrical properties. The high transparency enables them to absorb high light into the active layer to afford the hole-electron pairs generation, and the tuning of the Fermi levels with the donor allows the hole collection. Usually, the hole transport takes place in the HEL valence band, but in *n*-type metals such as MoO₃, it has been found that the conduction band facilitates the hole transport. Thus, the type of hole transport path will vary with the WF and energy levels of the inorganic and nanocarbon materials as HELs.

To meet and increase the hole transport efficiency, the inorganic and nanocarbon materials have been modified to tune the electronic and optical properties. It has changed the particles' size or added metal NPs to take advantage of the LSPR effect to increase the light absorption. Inorganic materials such as Mo, Ni were doped with V, Cu to tune the WF, increase conductivity and transparency, resulting in a high V_{oc}, FF, and J_{sc}. It has formed hybrid layers, such as MoS₂:MoO₃, to take advantage of the electron blocking of MoS₂ and the higher conductivity of MoO₃. Nanocarbon materials such as GO were doped with F₄TCNQ to induce a change in the WF by shifting the Fermi levels, resulting in an enhanced hole transport. Carbon nanotubes were functionalized with amino groups to increase the charge carrier properties and reduce R_s, improving FF and J_{sc}. HELs can also be subjected to ultraviolet ozone (UVO), annealing, and microwave-annealing post-treatments to increase V_{oc}, FF, and J_{sc} due to the reduction of oxygen defects in the surface morphology.

Additionally, it has improved the deposition techniques to facilitate the commercialization of these photovoltaic devices. Compared to the conventional spin coating technique, laser-assisted and electrospray allow the control of the surface morphology and thickness at low temperatures and short-times processing. The roll-to-roll technique is also attractive for large industrial-scale manufacturing of metal oxides, such as the inkjet printing of NiO_x. Overall, inorganic and

nanocarbon HELs are very favorable for OSCs, mainly because of their highest stability, improved electrical properties, and transparency in the visible range. The continuous investigation of a vast number of new inorganic and nanocarbon HELs, which can assure high efficiency, high stability, low costs, facile preparation, and improved film-forming properties over large areas, is essential to their future commercialization in OSCs.

Recommendations

Currently, it is known that inorganic and carbon-based materials can be composited or doped to improve their performance as HELs. It can design materials with specific structures and compositions to improve the OSC performance by changing the electronic level structure or varying the processing methods. However, the main limitation to the high PCE in OSCs is the complex physical process in the photoelectric conversion process. Thus, an understanding of the mechanisms involved with the changes in the chemical structure of the HELs is needed. This detailed analysis will require theoretical research to understand the current pathway and the influence of electrodes, HELs, active layers, and environmental conditions on OSCs' overall performance.

Furthermore, it should perform analysis in applying electrochemistry to develop new materials as HELs in OSCs. This technique offers the advantage of taking control during deposition and the HEL properties without involving high costs and environmental impacts. The development of multilayers that can act as anode and interfacial layers also offers new advances in photovoltaic devices, so the understanding between interfacial properties and material design through the synthesis will promise new materials for BHJ OSCs. OSCs' efficiency and stability will also improve with new architecture proposals such as tandem solar cells. Since the architecture comprises interfacial layers, an active layer, and electrodes, interfacial properties' optimization is essential to achieve OSCs' high efficiencies. The interfacial layers should be resistant to the active layer's solvent, stable to environmental conditions, and mechanical stress in flexible OSCs.

References

1. Fouquet, R. Historical energy transitions: Speed, prices and system transformation. *Energy Res. Soc. Sci.* **22**, 7–12 (2016).
2. Nematollahi, O., Hoghooghi, H., Rasti, M. & Sedaghat, A. Energy demands and renewable energy resources in the Middle East. *Renew. Sustain. Energy Rev.* **54**, 1172–1181 (2016).
3. Lifset, R. D. A new understanding of the American energy crisis of the 1970s. *Hist. Soc. Res.* **39**, 22–42 (2014).
4. Gregory, K. & Rogner, H. H. Energy resources and conversion technologies for the 21(st) century. *Mitig. Adapt. Strateg. Glob. Chang.* **3**, 171–230 (1998).
5. Gray, V. The IPCC future projections: are they plausible? *Clim. Res.* **10**, 155–162 (1998).
6. Höök, M. & Tang, X. Depletion of fossil fuels and anthropogenic climate change—A review. *Energy Policy* **52**, 797–809 (2013).
7. Turner, J. A. A Realizable Renewable Energy Future. *Science (80-)*. **285**, 687–689 (1999).
8. Poliakoff, M., Leitner, W. & Streng, E. S. The Twelve Principles of CO₂ CHEMISTRY. *Faraday Discuss.* **183**, 9–17 (2015).
9. Owusu, P. A. & Asumadu-Sarkodie, S. A review of renewable energy sources, sustainability issues and climate change mitigation. *Cogent Eng.* **3**, 1167990 (2016).
10. Ellabban, O., Abu-Rub, H. & Blaabjerg, F. Renewable energy resources: Current status, future prospects and their enabling technology. *Renew. Sustain. Energy Rev.* **39**, 748–764 (2014).
11. Luqman, M. *et al.* Estimation of Solar Energy Potential from Rooftop of Punjab Government Servants Cooperative Housing Society Lahore Using GIS. *Smart Grid Renew. Energy* **06**, 128–139 (2015).
12. Kabir, E., Kumar, P., Kumar, S., Adelodun, A. A. & Kim, K.-H. Solar energy: Potential and future prospects. *Renew. Sustain. Energy Rev.* **82**, 894–900 (2018).
13. Hosenuzzaman, M. *et al.* Global prospects, progress, policies, and environmental impact of solar photovoltaic power generation. *Renew. Sustain. Energy Rev.* **41**, 284–297 (2015).

14. Kannan, N. & Vakeesan, D. Solar energy for future world: - A review. *Renew. Sustain. Energy Rev.* **62**, 1092–1105 (2016).
15. Goswami, D. Y., Vijayaraghavan, S., Lu, S. & Tamm, G. New and emerging developments in solar energy. *Sol. Energy* **76**, 33–43 (2004).
16. Li, G., Zhu, R. & Yang, Y. Polymer solar cells. *Nat. Photonics* **6**, 153–161 (2012).
17. Lin, Y. *et al.* Metallic surface doping of metal halide perovskites. *Nat. Commun.* **12**, 7 (2021).
18. Rehman, S. ur *et al.* Synthesis of polyvinyl acetate /graphene nanocomposite and its application as an electrolyte in dye sensitized solar cells. *Optik (Stuttg.)*. **202**, 163591 (2020).
19. Liu, M., Johnston, M. B. & Snaith, H. J. Efficient planar heterojunction perovskite solar cells by vapour deposition. *Nature* **501**, 395–398 (2013).
20. Mathew, S. *et al.* Dye-sensitized solar cells with 13% efficiency achieved through the molecular engineering of porphyrin sensitizers. *Nat. Chem.* **6**, 242–247 (2014).
21. Liu, S. *et al.* High-efficiency organic solar cells with low non-radiative recombination loss and low energetic disorder. *Nat. Photonics* **14**, 300–305 (2020).
22. Chuang, C.-H. M., Brown, P. R., Bulović, V. & Bawendi, M. G. Improved performance and stability in quantum dot solar cells through band alignment engineering. *Nat. Mater.* **13**, 796–801 (2014).
23. Yin, Z., Wei, J. & Zheng, Q. Interfacial Materials for Organic Solar Cells: Recent Advances and Perspectives. *Adv. Sci.* **3**, 1500362 (2016).
24. Green, M. A. Recent developments in photovoltaics. *Sol. Energy* **76**, 3–8 (2004).
25. Chamberlain, G. A. Organic solar cells: A review. *Sol. Cells* **8**, 47–83 (1983).
26. Günes, S., Neugebauer, H. & Sariciftci, N. S. Conjugated Polymer-Based Organic Solar Cells. *Chem. Rev.* **107**, 1324–1338 (2007).
27. Dennler, G., Scharber, M. C. & Brabec, C. J. Polymer-Fullerene Bulk-Heterojunction Solar Cells. *Adv. Mater.* **21**, 1323–1338 (2009).
28. Liu, Q. *et al.* 18% Efficiency organic solar cells. *Sci. Bull.* **65**, 272–275 (2020).
29. Zhao, W. *et al.* Molecular Optimization Enables over 13% Efficiency in Organic Solar Cells. *J. Am. Chem. Soc.* **139**, 7148–7151 (2017).
30. Hou, J., Inganäs, O., Friend, R. H. & Gao, F. Organic solar cells based on non-fullerene acceptors. *Nature Materials* **17**, 119–128 (2018).
31. BERNÈDE, J. C. ORGANIC PHOTOVOLTAIC CELLS: HISTORY, PRINCIPLE AND TECHNIQUES. *J. Chil. Chem. Soc.* **53**, (2008).

32. Kearns, D. & Calvin, M. Photovoltaic Effect and Photoconductivity in Laminated Organic Systems. *J. Chem. Phys.* **29**, 950–951 (1958).
33. Tang, C. W. Two-layer organic photovoltaic cell. *Appl. Phys. Lett.* **48**, 183–185 (1986).
34. Sariciftci, N. S., Smilowitz, L., Heeger, A. J. & Wudl, F. Semiconducting polymers (as donors) and buckminsterfullerene (as acceptor): photoinduced electron transfer and heterojunction devices. *Synth. Met.* **59**, 333–352 (1993).
35. Yu, G., Gao, J., Hummelen, J. C., Wudl, F. & Heeger, A. J. Polymer Photovoltaic Cells: Enhanced Efficiencies via a Network of Internal Donor-Acceptor Heterojunctions. *Science (80-.)*. **270**, 1789–1791 (1995).
36. Li, Y. Molecular Design of Photovoltaic Materials for Polymer Solar Cells: Toward Suitable Electronic Energy Levels and Broad Absorption. *Acc. Chem. Res.* **45**, 723–733 (2012).
37. Yao, H. *et al.* Molecular Design of Benzodithiophene-Based Organic Photovoltaic Materials. *Chem. Rev.* **116**, 7397–7457 (2016).
38. Kim, J. Y. *et al.* Efficient Tandem Polymer Solar Cells Fabricated by All-Solution Processing. *Science (80-.)*. **317**, 222–225 (2007).
39. Meillaud, F., Shah, A., Droz, C., Vallat-Sauvain, E. & Miazza, C. Efficiency limits for single-junction and tandem solar cells. *Sol. Energy Mater. Sol. Cells* **90**, 2952–2959 (2006).
40. Lee, Y.-J., Adkison, B. L., Xu, L., Kramer, A. A. & Hsu, J. W. P. Comparison of conventional and inverted organic photovoltaic devices with controlled illumination area and extraction layers. *Sol. Energy Mater. Sol. Cells* **144**, 592–599 (2016).
41. Lai, T.-H., Tsang, S.-W., Manders, J. R., Chen, S. & So, F. Properties of interlayer for organic photovoltaics. *Mater. Today* **16**, 424–432 (2013).
42. Clarke, T. M. & Durrant, J. R. Charge Photogeneration in Organic Solar Cells. *Chem. Rev.* **110**, 6736–6767 (2010).
43. Nunzi, J.-M. Organic photovoltaic materials and devices. *Comptes Rendus Phys.* **3**, 523–542 (2002).
44. Wang, T. *et al.* Fabricating High Performance, Donor-Acceptor Copolymer Solar Cells by Spray-Coating in Air. *Adv. Energy Mater.* **3**, 505–512 (2013).
45. Krebs, F. C. Fabrication and processing of polymer solar cells: A review of printing and coating techniques. *Sol. Energy Mater. Sol. Cells* **93**, 394–412 (2009).
46. Zhitomirsky, I., Niewczas, M. & Petric, A. Electrodeposition of hybrid organic–

- inorganic films containing iron oxide. *Mater. Lett.* **57**, 1045–1050 (2003).
47. Krebs, F. C. Polymer solar cell modules prepared using roll-to-roll methods: Knife-over-edge coating, slot-die coating and screen printing. *Sol. Energy Mater. Sol. Cells* **93**, 465–475 (2009).
 48. Jung, J. W. & Jo, W. H. Annealing-Free High Efficiency and Large Area Polymer Solar Cells Fabricated by a Roller Painting Process. *Adv. Funct. Mater.* **20**, 2355–2363 (2010).
 49. Shrotriya, V. *et al.* Accurate Measurement and Characterization of Organic Solar Cells. *Adv. Funct. Mater.* **16**, 2016–2023 (2006).
 50. Qi, B. & Wang, J. Fill factor in organic solar cells. *Phys. Chem. Chem. Phys.* **15**, 8972 (2013).
 51. Yip, H.-L. & Jen, A. K. Y. Recent advances in solution-processed interfacial materials for efficient and stable polymer solar cells. *Energy Environ. Sci.* **5**, 5994 (2012).
 52. Koster, L. J. A., Mihailetschi, V. D., Xie, H. & Blom, P. W. M. Origin of the light intensity dependence of the short-circuit current of polymer/fullerene solar cells. *Appl. Phys. Lett.* **87**, 203502 (2005).
 53. Parker, I. D. Carrier tunneling and device characteristics in polymer light-emitting diodes. *J. Appl. Phys.* **75**, 1656–1666 (1994).
 54. Elumalai, N. K. & Uddin, A. Open circuit voltage of organic solar cells: an in-depth review. *Energy Environ. Sci.* **9**, 391–410 (2016).
 55. Ratcliff, E. L., Zacher, B. & Armstrong, N. R. Selective Interlayers and Contacts in Organic Photovoltaic Cells. *J. Phys. Chem. Lett.* **2**, 1337–1350 (2011).
 56. Mihailetschi, V. D., Blom, P. W. M., Hummelen, J. C. & Rispens, M. T. Cathode dependence of the open-circuit voltage of polymer:fullerene bulk heterojunction solar cells. *J. Appl. Phys.* **94**, 6849–6854 (2003).
 57. Street, R. A., Song, K. W. & Cowan, S. Influence of series resistance on the photocurrent analysis of organic solar cells. *Org. Electron.* **12**, 244–248 (2011).
 58. Servaites, J. D., Yeganeh, S., Marks, T. J. & Ratner, M. A. Efficiency Enhancement in Organic Photovoltaic Cells: Consequences of Optimizing Series Resistance. *Adv. Funct. Mater.* **20**, 97–104 (2010).
 59. Proctor, C. M. & Nguyen, T.-Q. Effect of leakage current and shunt resistance on the light intensity dependence of organic solar cells. *Appl. Phys. Lett.* **106**, 083301 (2015).
 60. Wurfel, U., Cuevas, A. & Wurfel, P. Charge Carrier Separation in Solar Cells. *IEEE J. Photovoltaics* **5**, 461–469 (2015).

61. Po, R., Carbonera, C., Bernardi, A. & Camaioni, N. The role of buffer layers in polymer solar cells. *Energy Environ. Sci.* **4**, 285–310 (2011).
62. Steim, R., Kogler, F. R. & Brabec, C. J. Interface materials for organic solar cells. *J. Mater. Chem.* **20**, 2499 (2010).
63. Braun, S., Salaneck, W. R. & Fahlman, M. Energy-Level Alignment at Organic/Metal and Organic/Organic Interfaces. *Adv. Mater.* **21**, 1450–1472 (2009).
64. Tokito, S., Noda, K. & Taga, Y. Metal oxides as a hole-injecting layer for an organic electroluminescent device. *J. Phys. D. Appl. Phys.* **29**, 2750–2753 (1996).
65. Meyer, J. *et al.* Transition Metal Oxides for Organic Electronics: Energetics, Device Physics and Applications. *Adv. Mater.* **24**, 5408–5427 (2012).
66. Chen, L.-M., Xu, Z., Hong, Z. & Yang, Y. Interface investigation and engineering – achieving high performance polymer photovoltaic devices. *J. Mater. Chem.* **20**, 2575 (2010).
67. Curiel, D. & Más-Montoya, M. Hole Transporting Layers in Printable Solar Cells. in *Printable Solar Cells* 93–161 (John Wiley & Sons, Inc., 2017). doi:10.1002/9781119283720.ch4
68. Shrotriya, V., Li, G., Yao, Y., Chu, C.-W. & Yang, Y. Transition metal oxides as the buffer layer for polymer photovoltaic cells. *Appl. Phys. Lett.* **88**, 073508 (2006).
69. Han, S. *et al.* Improving performance of organic solar cells using amorphous tungsten oxides as an interfacial buffer layer on transparent anodes. *Org. Electron.* **10**, 791–797 (2009).
70. Irwin, M. D., Buchholz, D. B., Hains, A. W., Chang, R. P. H. & Marks, T. J. p-Type semiconducting nickel oxide as an efficiency-enhancing anode interfacial layer in polymer bulk-heterojunction solar cells. *Proc. Natl. Acad. Sci.* **105**, 2783–2787 (2008).
71. Wang, K. *et al.* Solution-Processed Fe₃O₄ Magnetic Nanoparticle Thin Film Aligned by an External Magnetostatic Field as a Hole Extraction Layer for Polymer Solar Cells. *ACS Appl. Mater. Interfaces* **5**, 10325–10330 (2013).
72. Gu, X. *et al.* A Solution-Processed Hole Extraction Layer Made from Ultrathin MoS₂ Nanosheets for Efficient Organic Solar Cells. *Adv. Energy Mater.* **3**, 1262–1268 (2013).
73. Xu, H. *et al.* Hole transport layers for organic solar cells: Recent progress and prospects. *Journal of Materials Chemistry A* **8**, 11478–11492 (2020).
74. Kawano, K. *et al.* Degradation of organic solar cells due to air exposure. *Sol. Energy Mater. Sol. Cells* **90**, 3520–3530 (2006).

75. Fouquet, R. The demand for environmental quality in driving transitions to low-polluting energy sources. *Energy Policy* **50**, 138–149 (2012).
76. Machol, B. & Rizk, S. Economic value of U.S. fossil fuel electricity health impacts. *Environ. Int.* **52**, 75–80 (2013).
77. Fouquet, R. A Brief History of Energy. in *Solar Revolution* (The MIT Press, 2006). doi:10.7551/mitpress/6331.003.0006
78. Florides, G. A. & Christodoulides, P. Global warming and carbon dioxide through sciences. *Environ. Int.* **35**, 390–401 (2009).
79. Sleep, N. H. & Zahnle, K. Carbon dioxide cycling and implications for climate on ancient Earth. *J. Geophys. Res. Planets* **106**, 1373–1399 (2001).
80. Levine, U. Y., Teal, T. K., Robertson, G. P. & Schmidt, T. M. Agriculture's impact on microbial diversity and associated fluxes of carbon dioxide and methane. *ISME J.* **5**, 1683–1691 (2011).
81. Kerr, R. A. CLIMATE CHANGE: Global Warming Is Changing the World. *Science* (80-.). **316**, 188–190 (2007).
82. De Schryver, A. M., Brakkee, K. W., Goedkoop, M. J. & Huijbregts, M. A. J. Characterization Factors for Global Warming in Life Cycle Assessment Based on Damages to Humans and Ecosystems. *Environ. Sci. Technol.* **43**, 1689–1695 (2009).
83. Oelkers, E. H. & Cole, D. R. Carbon Dioxide Sequestration A Solution to a Global Problem. *Elements* **4**, 305–310 (2008).
84. Jäger-Waldau, A. Photovoltaics: Status and Perspectives until 2020. *Green* **1**, (2011).
85. Kang, H. *et al.* Bulk-Heterojunction Organic Solar Cells: Five Core Technologies for Their Commercialization. *Advanced Materials* **28**, (2016).
86. Riede, M., Spoltore, D. & Leo, K. Organic Solar Cells—The Path to Commercial Success. *Adv. Energy Mater.* **11**, 2002653 (2021).
87. Yang, B. *et al.* Over 100-nm-Thick MoO₃ Films with Superior Hole Collection and Transport Properties for Organic Solar Cells. *Adv. Energy Mater.* **8**, 1800698 (2018).
88. Lou, X. W. & Zeng, H. C. Complex α -MoO₃ Nanostructures with External Bonding Capacity for Self-Assembly. *J. Am. Chem. Soc.* **125**, 2697–2704 (2003).
89. Pan, W. *et al.* Structure, Optical, and Catalytic Properties of Novel Hexagonal Metastable α -MoO₃ Nano- and Microrods Synthesized with Modified Liquid-Phase Processes. *Chem. Mater.* **22**, 6202–6208 (2010).
90. Kyaw, A. K. K. *et al.* An inverted organic solar cell employing a sol-gel derived ZnO electron selective layer and thermal evaporated MoO₃ hole selective layer. *Appl. Phys.*

- Lett.* **93**, 221107 (2008).
91. Lee, D. *et al.* Enhanced Operating Temperature Stability of Organic Solar Cells with Metal Oxide Hole Extraction Layer. *Polymers (Basel)*. **12**, 992 (2020).
 92. Liao, X. *et al.* Tunability of MoO₃ Thin-Film Properties Due to Annealing in Situ Monitored by Hard X-ray Photoemission. *ACS Omega* **4**, 10985–10990 (2019).
 93. Boudaoud, L., Benramdane, N., Desfeux, R., Khelifa, B. & Mathieu, C. Structural and optical properties of MoO₃ and V₂O₅ thin films prepared by Spray Pyrolysis. *Catal. Today* **113**, (2006).
 94. Inzani, K. *et al.* Tailoring properties of nanostructured MoO_{3-x} thin films by aqueous solution deposition. *Appl. Surf. Sci.* **459**, 822–829 (2018).
 95. Bortoti, A. A., Gavanski, A. de F., Velazquez, Y. R., Galli, A. & de Castro, E. G. Facile and low cost oxidative conversion of MoS₂ in α -MoO₃: Synthesis, characterization and application. *J. Solid State Chem.* **252**, 111–118 (2017).
 96. Ji, R., Cheng, J., Yang, X., Yu, J. & Li, L. Enhanced charge carrier transport in spray-cast organic solar cells using solution processed MoO₃ micro arrays. *RSC Adv.* **7**, 3059–3065 (2017).
 97. Wang, Y. *et al.* Efficient and stable operation of nonfullerene organic solar cells: retaining a high built-in potential. *J. Mater. Chem. A* **8**, 21255–21264 (2020).
 98. Kim, J.-H. *et al.* Improving charge transport of P3HT:PCBM organic solar cell using MoO₃ nanoparticles as an interfacial buffer layer. *Electron. Mater. Lett.* **12**, 383–387 (2016).
 99. Choy, W. C. H. & Xingang Ren. Plasmon-Electrical Effects on Organic Solar Cells by Incorporation of Metal Nanostructures. *IEEE J. Sel. Top. Quantum Electron.* **22**, 1–9 (2016).
 100. Bobeico, E. *et al.* Evaporated MoO_x as General Back-Side Hole Collector for Solar Cells. *Coatings* **10**, 763 (2020).
 101. Jagadamma, L. K. *et al.* Solution-processable MoO_x nanocrystals enable highly efficient reflective and semitransparent polymer solar cells. *Nano Energy* **28**, 277–287 (2016).
 102. Wang, J. *et al.* Improved Performance of Polymer Solar Cells by Thermal Evaporation of AgAl Alloy Nanostructures into the Hole-Transport Layer. *ACS Appl. Mater. Interfaces* **8**, 26098–26104 (2016).
 103. Cong, S. *et al.* Modifying the valence state of molybdenum in the efficient oxide buffer layer of organic solar cells via a mild hydrogen peroxide treatment. *J. Mater.*

- Chem. C* **5**, 889–895 (2017).
104. Jung, S., Lee, J., Kim, U. & Park, H. Solution-Processed Molybdenum Oxide with Hydroxyl Radical-Induced Oxygen Vacancy as an Efficient and Stable Interfacial Layer for Organic Solar Cells. *Sol. RRL* **4**, 1900420 (2020).
 105. Kobori, T., Kamata, N. & Fukuda, T. Effect of annealing-induced oxidation of molybdenum oxide on organic photovoltaic device performance. *Org. Electron.* **37**, 126–133 (2016).
 106. Li, Y., Yu, H., Huang, X., Wu, Z. & Chen, M. A simple synthesis method to prepare a molybdenum oxide hole-transporting layer for efficient polymer solar cells. *RSC Adv.* **7**, 7890–7900 (2017).
 107. Soultati, A. *et al.* Dehydration of molybdenum oxide hole extraction layers via microwave annealing for the improvement of efficiency and lifetime in organic solar cells. *J. Mater. Chem. C* **4**, 7683–7694 (2016).
 108. Cheng, F., Wu, Y., Shen, Y., Cai, X. & Li, L. Enhancing the performance and stability of organic solar cells using solution processed MoO₃ as hole transport layer. *RSC Adv.* **7**, 37952–37958 (2017).
 109. Cai, P. *et al.* An Ultraviolet-Deposited MoO₃ Film as Anode Interlayer for High-Performance Polymer Solar Cells. *Adv. Mater. Interfaces* **7**, 1901912 (2020).
 110. Tran, H. N. *et al.* 17% Non-Fullerene Organic Solar Cells with Annealing-Free Aqueous MoO_x. *Adv. Sci.* **7**, 2002395 (2020).
 111. Irfan *et al.* Energy level evolution of air and oxygen exposed molybdenum trioxide films. *Appl. Phys. Lett.* **96**, 243307 (2010).
 112. Vasilopoulou, M., Soultati, A., Argitis, P., Stergiopoulos, T. & Davazoglou, D. Fast Recovery of the High Work Function of Tungsten and Molybdenum Oxides via Microwave Exposure for Efficient Organic Photovoltaics. *J. Phys. Chem. Lett.* **5**, 1871–1879 (2014).
 113. Chang, F.-K., Huang, Y.-C., Jeng, J.-S. & Chen, J.-S. Band offset of vanadium-doped molybdenum oxide hole transport layer in organic photovoltaics. *Solid. State. Electron.* **122**, 18–22 (2016).
 114. Marchal, W. *et al.* Steering the properties of MoO_x hole transporting layers in OPVs and OLEDs: Interface morphology vs. electronic structure. *Materials (Basel)*. **10**, 123 (2017).
 115. Bai, Y. *et al.* Enhancing the electron blocking ability of *n*-type MoO₃ by doping with *p*-type NiO for efficient nonfullerene polymer solar cells. *Org. Electron.* **68**, 168–175

- (2019).
116. Yoon, S. *et al.* Enhanced hole extraction by interaction between CuI and MoO₃ in the hole transport layer of organic photovoltaic devices. *Org. Electron.* **32**, 200–207 (2016).
 117. Li, Z. *et al.* Impedance investigation of the highly efficient polymer solar cells with composite CuBr₂/MoO₃ hole transport layer. *Phys. Chem. Chem. Phys.* **19**, 20839–20846 (2017).
 118. Li, Y., Yu, H., Huang, X., Wu, Z. & Xu, H. Improved performance for polymer solar cells using CTAB-modified MoO₃ as an anode buffer layer. *Sol. Energy Mater. Sol. Cells* **171**, 72–84 (2017).
 119. Kang, Q. *et al.* An inorganic molecule-induced electron transfer complex for highly efficient organic solar cells. *J. Mater. Chem. A* **8**, 5580–5586 (2020).
 120. Kwon, K. C. *et al.* Synthesis of atomically thin alloyed molybdenum-tungsten disulfides thin films as hole transport layers in organic light-emitting diodes. *Appl. Surf. Sci.* **541**, 148529 (2021).
 121. Cheng, P.-P. *et al.* Light trapping enhancement of inverted polymer solar cells with a nanostructured scattering rear electrode. *Org. Electron.* **14**, 2158–2163 (2013).
 122. Zhang, W., Lan, W., Lee, M. H., Singh, J. & Zhu, F. A versatile solution-processed MoO₃/Au nanoparticles/MoO₃ hole contact for high performing PEDOT:PSS-free organic solar cells. *Org. Electron.* **52**, 1–6 (2018).
 123. Hofmann, M., Hofmann, H., Hagelüken, C. & Hool, A. Critical raw materials: A perspective from the materials science community. *Sustain. Mater. Technol.* **17**, e00074 (2018).
 124. Chen, S., Dai, Y., Zhao, D. & Zhang, H. ITO-free flexible organic photovoltaics with multilayer MoO₃/LiF/MoO₃/Ag/MoO₃ as the transparent electrode. *Semicond. Sci. Technol.* **31**, 055013 (2016).
 125. Lee, H.-M., Kim, S.-S. & Kim, H.-K. Artificially MoO₃ graded ITO anodes for acidic buffer layer free organic photovoltaics. *Appl. Surf. Sci.* **364**, 340–348 (2016).
 126. Sun, J. *et al.* Comparing molybdenum oxide thin films prepared by magnetron sputtering and thermal evaporation applied in organic solar cells. *J. Mater. Sci. Mater. Electron.* **27**, 3245–3249 (2016).
 127. Chaturvedi, N., Swami, S. K. & Dutta, V. Electric field assisted spray deposited MoO₃ thin films as a hole transport layer for organic solar cells. *Sol. Energy* **137**, 379–384

- (2016).
128. Dong, W. J., Ham, J., Jung, G. H., Son, J. H. & Lee, J.-L. Ultrafast laser-assisted synthesis of hydrogenated molybdenum oxides for flexible organic solar cells. *J. Mater. Chem. A* **4**, 4755–4762 (2016).
 129. Meyer, J. *et al.* Highly efficient simplified organic light emitting diodes. *Appl. Phys. Lett.* **91**, 113506 (2007).
 130. Tao, C. *et al.* Role of tungsten oxide in inverted polymer solar cells. *Appl. Phys. Lett.* **94**, 043311 (2009).
 131. Miyake, K., Kaneko, H., Sano, M. & Suedomi, N. Physical and electrochromic properties of the amorphous and crystalline tungsten oxide thick films prepared under reducing atmosphere. *J. Appl. Phys.* **55**, 2747–2753 (1984).
 132. Vida, G., Josepovits, V. K., Győr, M. & Deák, P. Characterization of Tungsten Surfaces by Simultaneous Work Function and Secondary Electron Emission Measurements. *Microsc. Microanal.* **9**, 337–342 (2003).
 133. Stubhan, T. *et al.* High Fill Factor Polymer Solar Cells Incorporating a Low Temperature Solution Processed WO₃ Hole Extraction Layer. *Adv. Energy Mater.* **2**, 1433–1438 (2012).
 134. Brabec, C. J. Organic photovoltaics: technology and market. *Sol. Energy Mater. Sol. Cells* **83**, 273–292 (2004).
 135. Lee, Y. H., Abdu H, A. E., Kim, D. H. & Kim, T. W. Enhancement of the power conversion efficiency of organic photovoltaic cells due to Au@SiO₂ core shell nanoparticles embedded into a WO₃ hole transport layer. *Org. Electron.* **68**, 182–186 (2019).
 136. Lee, Y. H., Kim, D. H. & Kim, T. W. Enhanced power conversion efficiency of organic photovoltaic devices due to the surface plasmonic resonance effect generated utilizing Au-WO₃ nanocomposites. *Org. Electron.* **45**, 256–262 (2017).
 137. Shen, W. *et al.* Enhanced efficiency of polymer solar cells by structure-differentiated silver nano-dopants in solution-processed tungsten oxide layer. *Mater. Sci. Eng. B* **206**, 61–68 (2016).
 138. Zheng, Z. *et al.* A Highly Efficient Non-Fullerene Organic Solar Cell with a Fill Factor over 0.80 Enabled by a Fine-Tuned Hole-Transporting Layer. *Adv. Mater.* **30**, 1801801 (2018).
 139. Remya, R., Gayathri, P. T. G. & Deb, B. Studies on solution-processed tungsten oxide nanostructures for efficient hole transport in the inverted polymer solar cells. *Mater.*

- Chem. Phys.* **255**, 123584 (2020).
140. Liao, H.-H., Chen, L.-M., Xu, Z., Li, G. & Yang, Y. Highly efficient inverted polymer solar cell by low temperature annealing of Cs₂CO₃ interlayer. *Appl. Phys. Lett.* **92**, 173303 (2008).
 141. Huang, J.-S. *et al.* Solution-processed vanadium oxide as an anode interlayer for inverted polymer solar cells hybridized with ZnO nanorods. *Org. Electron.* **10**, 1060–1065 (2009).
 142. Meyer, J., Zilberberg, K., Riedl, T. & Kahn, A. Electronic structure of Vanadium pentoxide: An efficient hole injector for organic electronic materials. *J. Appl. Phys.* **110**, 033710 (2011).
 143. Xu, M.-F. *et al.* Low-temperature, aqueous solution-processed V₂O₅ as the hole-transport layer for high performance organic solar cells. *J. Mater. Sci. Mater. Electron.* **29**, 14783–14787 (2018).
 144. Jiang, Y. *et al.* Enhancement of Photovoltaic Performance by Utilizing Readily Accessible Hole Transporting Layer of Vanadium(V) Oxide Hydrate in a Polymer-Fullerene Blend Solar Cell. *ACS Appl. Mater. Interfaces* (2016).
doi:10.1021/acsami.6b02824
 145. Cong, H. *et al.* Facile Approach to Preparing a Vanadium Oxide Hydrate Layer as a Hole-Transport Layer for High-Performance Polymer Solar Cells. *ACS Appl. Mater. Interfaces* **9**, 18087–18094 (2017).
 146. Xie, F. *et al.* Low-Temperature Solution-Processed Hydrogen Molybdenum and Vanadium Bronzes for an Efficient Hole-Transport Layer in Organic Electronics. *Adv. Mater.* **25**, 2051–2055 (2013).
 147. Vishnumurthy, K. A., Kesavan, A. V., Swathi, S. K. & Ramamurthy, P. C. Low band gap thienothiophene-diketopyrrolopyrrole copolymers with V₂O₅ as hole transport layer for photovoltaic application. *Opt. Mater. (Amst)*. **109**, 110303 (2020).
 148. Ravi, R. & Deb, B. Studies on One-Step-Synthesized Hydrated Vanadium Pentoxide for Efficient Hole Transport in Organic Photovoltaics. *Energy Technol.* **8**, 1901323 (2020).
 149. Xu, W. *et al.* Solution-processed VO_x prepared using a novel synthetic method as the hole extraction layer for polymer solar cells. *J. Mater. Chem. C* **4**, 1953–1958 (2016).
 150. Shafeeq, K. M., Athira, V. P., Kishor, C. H. R. & Aneesh, P. M. Structural and optical properties of V₂O₅ nanostructures grown by thermal decomposition technique. *Appl. Phys. A* **126**, 586 (2020).

151. Alsulami, A. *et al.* Thermally Stable Solution Processed Vanadium Oxide as a Hole Extraction Layer in Organic Solar Cells. *Materials (Basel)*. **9**, 235 (2016).
152. Zafar, M., Yun, J.-Y. & Kim, D.-H. Highly stable inverted organic photovoltaic cells with a V₂O₅ hole transport layer. *Korean J. Chem. Eng.* **34**, 1504–1508 (2017).
153. Teng, N.-W. *et al.* Highly Efficient Nonfullerene Organic Photovoltaic Devices with 10% Power Conversion Efficiency Enabled by a Fine-Tuned and Solution-Processed Hole-Transporting Layer. *Sol. RRL* **4**, 2000223 (2020).
154. Li, J. *et al.* Enhanced organic photovoltaic performance through promoting crystallinity of photoactive layer and conductivity of hole-transporting layer by V₂O₅ doped PEDOT:PSS hole-transporting layers. *Sol. Energy* **211**, 1102–1109 (2020).
155. Xia, C. *et al.* Metal-Organic Decomposition-Mediated Nanoparticulate Vanadium Oxide Hole Transporting Buffer Layer for Polymer Bulk-Heterojunction Solar Cells. *Polymers (Basel)*. **12**, 1791 (2020).
156. Beliatas, M. J. *et al.* Slot-Die-Coated V₂O₅ as Hole Transport Layer for Flexible Organic Solar Cells and Optoelectronic Devices. *Adv. Eng. Mater.* **18**, 1494–1503 (2016).
157. Arbab, E. A. A. & Mola, G. T. V₂O₅ thin film deposition for application in organic solar cells. *Appl. Phys. A Mater. Sci. Process.* (2016). doi:10.1007/s00339-016-9966-1
158. Kavuri, H. A. *et al.* Electro-spray-deposited vanadium oxide anode interlayers for high-efficiency organic solar cells. *Org. Electron.* **57**, 239–246 (2018).
159. Lee, D.-Y., Cho, S.-P., Na, S.-I. & Kim, S.-S. ITO-free polymer solar cells with vanadium oxide hole transport layer. *J. Ind. Eng. Chem.* **45**, 1–4 (2017).
160. Ko, E.-H. & Kim, H.-K. Highly transparent vanadium oxide-graded indium zinc oxide electrodes for flexible organic solar cells. *Thin Solid Films* **601**, 2–6 (2016).
161. Ai, L. *et al.* Influence of substrate temperature on electrical and optical properties of *p*-type semitransparent conductive nickel oxide thin films deposited by radio frequency sputtering. *Appl. Surf. Sci.* **254**, 2401–2405 (2008).
162. Manders, J. R. *et al.* Solution-Processed Nickel Oxide Hole Transport Layers in High Efficiency Polymer Photovoltaic Cells. *Adv. Funct. Mater.* **23**, 2993–3001 (2013).
163. Parthiban, S. *et al.* Enhanced efficiency and stability of polymer solar cells using solution-processed nickel oxide as hole transport material. *Curr. Appl. Phys.* **17**, 1232–1237 (2017).
164. Chavhan, S. D. *et al.* Low temperature processed NiO hole transport layers for efficient polymer solar cells. *Org. Electron.* **44**, 59–66 (2017).

165. Kim, J. K. PEG-assisted Sol-gel Synthesis of Compact Nickel Oxide Hole-Selective Layer with Modified Interfacial Properties for Organic Solar Cells. *Polymers (Basel)*. **11**, 120 (2019).
166. Rho, Y., Kang, K.-T. & Lee, D. Highly crystalline Ni/NiO hybrid electrodes processed by inkjet printing and laser-induced reductive sintering under ambient conditions. *Nanoscale* **8**, 8976–8985 (2016).
167. Singh, A., Gupta, S. K. & Garg, A. Inkjet printing of NiO films and integration as hole transporting layers in polymer solar cells. *Sci. Rep.* **7**, (2017).
168. Huang, S. *et al.* Enhancing the performance of polymer solar cells using solution-processed copper doped nickel oxide nanoparticles as hole transport layer. *J. Colloid Interface Sci.* **535**, 308–317 (2019).
169. Al-Jawhari, H. A., Caraveo-Frescas, J. A., Hedhili, M. N. & Alshareef, H. N. P-Type Cu₂O/SnO Bilayer Thin Film Transistors Processed at Low Temperatures. *ACS Appl. Mater. Interfaces* **5**, 9615–9619 (2013).
170. Murali, D. S. *et al.* Synthesis of Cu₂O from CuO thin films: Optical and electrical properties. *AIP Adv.* **5**, 047143 (2015).
171. Fortunato, E. *et al.* Thin-film transistors based on *p*-type Cu₂O thin films produced at room temperature. *Appl. Phys. Lett.* **96**, 192102 (2010).
172. Zuo, C. & Ding, L. Solution-Processed Cu₂O and CuO as Hole Transport Materials for Efficient Perovskite Solar Cells. *Small* **11**, 5528–5532 (2015).
173. Yu, Z. *et al.* An aqueous solution-processed CuO X film as an anode buffer layer for efficient and stable organic solar cells. *J. Mater. Chem. A* **4**, 5130–5136 (2016).
174. Yu, R.-S. & Tasi, C.-P. Structure, composition and properties of *p*-type CuCrO₂ thin films. *Ceram. Int.* **40**, 8211–8217 (2014).
175. Han, M. *et al.* Structural, electronic band transition and optoelectronic properties of delafossite CuGa_{1-x}Cr_xO₂ (0 ≤ x ≤ 1) solid solution films grown by the sol-gel method. *J. Mater. Chem.* **22**, 18463 (2012).
176. Xiong, D. *et al.* Hydrothermal synthesis of ultrasmall CuCrO₂ nanocrystal alternatives to NiO nanoparticles in efficient *p*-type dye-sensitized solar cells. *J. Mater. Chem.* **22**, 24760 (2012).
177. Marquardt, M. A., Ashmore, N. A. & Cann, D. P. Crystal chemistry and electrical properties of the delafossite structure. *Thin Solid Films* **496**, 146–156 (2006).
178. Wang, J., Lee, Y.-J. & Hsu, J. W. P. Sub-10 nm copper chromium oxide nanocrystals as a solution processed *p*-type hole transport layer for organic photovoltaics. *J. Mater.*

- Chem. C* **4**, 3607–3613 (2016).
179. Wang, J. *et al.* Combustion Synthesis of *p*-Type Transparent Conducting CuCrO_{2+x} and Cu:CrO_x Thin Films at 180 °C. *ACS Appl. Mater. Interfaces* **10**, 3732–3738 (2018).
 180. Wahl, T., Zellmer, S., Hanisch, J., Garnweitner, G. & Ahlswede, E. Thin indium tin oxide nanoparticle films as hole transport layer in inverted organic solar cells. *Thin Solid Films* **616**, 419–424 (2016).
 181. Bhargav, R., Gairola, S. P., Patra, A., Naqvi, S. & Dhawan, S. K. Improved performance of organic solar cells with solution processed hole transport layer. *Opt. Mater. (Amst)*. **80**, 138–142 (2018).
 182. Kan, M. *et al.* Structures and Phase Transition of a MoS_2 Monolayer. *J. Phys. Chem. C* **118**, 1515–1522 (2014).
 183. Barrera, D. *et al.* Inverted OPVs with MoS_2 hole transport layer deposited by spray coating. *Mater. Today Energy* **5**, 107–111 (2017).
 184. Martinez-Rojas, F. *et al.* $\text{Mo}(\text{S}_x\text{O}_y)$ thin films deposited by electrochemistry for application in organic photovoltaic cells. *Mater. Chem. Phys.* **201**, 331–338 (2017).
 185. Xing, W. *et al.* MoS_2 Quantum Dots with a Tunable Work Function for High-Performance Organic Solar Cells. *ACS Appl. Mater. Interfaces* **8**, 26916–26923 (2016).
 186. Wei, J., Yin, Z., Chen, S.-C., Cai, D. & Zheng, Q. Solution-processed MoS_x thin-films as hole-transport layers for efficient polymer solar cells. *RSC Adv.* **6**, 39137–39143 (2016).
 187. Adilbekova, B. *et al.* Liquid phase exfoliation of MoS_2 and WS_2 in aqueous ammonia and their application in highly efficient organic solar cells. *J. Mater. Chem. C* **8**, 5259–5264 (2020).
 188. Lin, Y. *et al.* 17% Efficient Organic Solar Cells Based on Liquid Exfoliated WS_2 as a Replacement for PEDOT:PSS. *Adv. Mater.* **31**, 1902965 (2019).
 189. Ram, K. S. & Singh, J. Over 20% Efficient and Stable Non-Fullerene-Based Ternary Bulk-Heterojunction Organic Solar Cell with WS_2 Hole-Transport Layer and Graded Refractive Index Antireflection Coating. *Adv. Theory Simulations* **3**, 2000047 (2020).
 190. Hilal, M. & Han, J. I. Preparation of hierarchical flower-like nickel sulfide as hole transporting material for organic solar cells via a one-step solvothermal method. *Sol. Energy* **188**, 403–413 (2019).
 191. Bhargav, R., Patra, A., Dhawan, S. K. & Gairola, S. P. Solution processed hole

- transport layer towards efficient and cost effective organic solar cells. *Sol. Energy* **165**, 131–135 (2018).
192. Jose, E., Mohan, M., Namboothiry, M. A. G. & Kumar, M. C. S. Room temperature deposition of high figure of merit *p*-type transparent conducting Cu–Zn–S thin films and their application in organic solar cells as an efficient hole transport layer. *J. Alloys Compd.* **829**, 154507 (2020).
 193. Wang, Z. *et al.* Energy level engineering of PEDOT:PSS by antimonene quantum sheet doping for highly efficient OLEDs. *J. Mater. Chem. C* **8**, 1796–1802 (2020).
 194. Wang, Z. *et al.* Novel 2D material from AMQS-based defect engineering for efficient and stable organic solar cells. *2D Mater.* **6**, 045017 (2019).
 195. Wijeyasinghe, N. *et al.* *p*-Doping of Copper(I) Thiocyanate (CuSCN) Hole-Transport Layers for High-Performance Transistors and Organic Solar Cells. *Adv. Funct. Mater.* **28**, 1802055 (2018).
 196. Dong, J. *et al.* A Low-Temperature Solution-Processed CuSCN/Polymer Hole Transporting Layer Enables High Efficiency for Organic Solar Cells. *ACS Appl. Mater. Interfaces* **12**, 46373–46380 (2020).
 197. Wang, Z. *et al.* Hybrid Hole Extraction Layer Enabled High Efficiency in Polymer Solar Cells. *ACS Appl. Mater. Interfaces* **12**, 55342–55348 (2020).
 198. Worakajit, P. *et al.* Elucidating the Coordination of Diethyl Sulfide Molecules in Copper(I) Thiocyanate (CuSCN) Thin Films and Improving Hole Transport by Antisolvent Treatment. *Adv. Funct. Mater.* **30**, 2002355 (2020).
 199. Suresh Kumar, M., Mohanta, K. & Batabyal, S. K. Solution processed Cu₂CdSnS₄ as a low-cost inorganic hole transport material for polymer solar cells. *Sol. Energy Mater. Sol. Cells* **161**, 157–161 (2017).
 200. Bourgeteau, T. *et al.* All solution-processed organic photocathodes with increased efficiency and stability via the tuning of the hole-extracting layer. *J. Mater. Chem. A* **4**, 4831–4839 (2016).
 201. Xu, Z. Fundamental Properties of Graphene. in *Graphene* 73–102 (Elsevier, 2018). doi:10.1016/B978-0-12-812651-6.00004-5
 202. Konkana, B. & Vasudevan, S. Understanding Aqueous Dispersibility of Graphene Oxide and Reduced Graphene Oxide through *p* K a Measurements. *J. Phys. Chem. Lett.* **3**, 867–872 (2012).
 203. Mattevi, C. *et al.* Evolution of Electrical, Chemical, and Structural Properties of Transparent and Conducting Chemically Derived Graphene Thin Films. *Adv. Funct.*

- Mater.* **19**, 2577–2583 (2009).
204. Sun, L. Structure and synthesis of graphene oxide. *Chinese J. Chem. Eng.* **27**, 2251–2260 (2019).
 205. Rafique, S. *et al.* Bulk Heterojunction Organic Solar Cells with Graphene Oxide Hole Transport Layer: Effect of Varied Concentration on Photovoltaic Performance. *J. Phys. Chem. C* **121**, 140–146 (2017).
 206. Allen, M. J., Tung, V. C. & Kaner, R. B. Honeycomb Carbon: A Review of Graphene. *Chem. Rev.* **110**, 132–145 (2010).
 207. Huang, X., Yu, H., Wu, Z. & Li, Y. Improving the performance of polymer solar cells by efficient optimizing the hole transport layer-graphene oxide. *J. Solid State Electrochem.* **22**, 317–329 (2018).
 208. Lee, S., Yeo, J.-S., Yun, J.-M. & Kim, D.-Y. Water dispersion of reduced graphene oxide stabilized via fullerene semiconductor for organic solar cells. *Opt. Mater. Express* **7**, 2487 (2017).
 209. Kwon, S.-N., Jung, C.-H. & Na, S.-I. Electron-beam-induced reduced graphene oxide as an alternative hole-transporting interfacial layer for high-performance and reliable polymer solar cells. *Org. Electron.* **34**, 67–74 (2016).
 210. Fakharan, Z., Naji, L. & Madanipour, K. Nd:YAG pulsed laser production of reduced-graphene oxide as hole transporting layer in polymer solar cells and the influences of solvent type. *Org. Electron.* **76**, 105459 (2020).
 211. Dericiler, K., Alishah, H. M., Bozar, S., Güneş, S. & Kaya, F. A novel method for graphene synthesis via electrochemical process and its utilization in organic photovoltaic devices. *Appl. Phys. A* **126**, 904 (2020).
 212. Xia, Y. *et al.* Graphene Oxide by UV-Ozone Treatment as an Efficient Hole Extraction Layer for Highly Efficient and Stable Polymer Solar Cells. *ACS Appl. Mater. Interfaces* **9**, 26252–26256 (2017).
 213. Rafique, S. *et al.* Moderately reduced graphene oxide via UV-ozone treatment as hole transport layer for high efficiency organic solar cells. *Org. Electron.* **59**, 140–148 (2018).
 214. Zhao, F.-G. *et al.* Sulfanilic Acid Pending on a Graphene Scaffold: Novel, Efficient Synthesis and Much Enhanced Polymer Solar Cell Efficiency and Stability Using It as a Hole Extraction Layer. *ACS Appl. Mater. Interfaces* **10**, 24679–24688 (2018).
 215. Ali, A. *et al.* Simultaneous reduction and sulfonation of graphene oxide for efficient hole selectivity in polymer solar cells. *Curr. Appl. Phys.* **18**, 599–610 (2018).

216. Chen, X. *et al.* Noncovalent phosphorylation of graphene oxide with improved hole transport in high-efficiency polymer solar cells. *Nanoscale* **10**, 14840–14846 (2018).
217. Cheng, X. *et al.* Fluorinated Reduced Graphene Oxide as an Efficient Hole-Transport Layer for Efficient and Stable Polymer Solar Cells. *ACS Omega* **2**, 2010–2016 (2017).
218. Nicasio-Collazo, J. *et al.* Functionalized and reduced graphene oxide as hole transport layer and for use in ternary organic solar cell. *Opt. Mater. (Amst)*. **98**, 109434 (2019).
219. Park, J.-J. *et al.* Orthogonal Printable Reduced Graphene Oxide 2D Materials as Hole Transport Layers for High-Performance Inverted Polymer Solar Cells: Sheet Size Effect on Photovoltaic Properties. *ACS Appl. Mater. Interfaces* **12**, 42811–42820 (2020).
220. Zheng, X. *et al.* Solution-processed Graphene-MoS₂ heterostructure for efficient hole extraction in organic solar cells. *Carbon N. Y.* **142**, 156–163 (2019).
221. Shoyiga, H. O., Martincigh, B. S. & Nyamori, V. O. Hydrothermal synthesis of reduced graphene oxide-anatase titania nanocomposites for dual application in organic solar cells. *Int. J. Energy Res.* er.6313 (2020). doi:10.1002/er.6313
222. Lee, J. H. *et al.* Improved performance of organic photovoltaic devices by doping F₄TCNQ onto solution-processed graphene as a hole transport layer. *Org. Electron.* **30**, 302–311 (2016).
223. Lee, C. K. *et al.* Versatile and Tunable Electrical Properties of Doped Nonoxidized Graphene Using Alkali Metal Chlorides. *ACS Appl. Mater. Interfaces* **11**, 42520–42527 (2019).
224. Sun, B. *et al.* Copper(II) chloride doped graphene oxides as efficient hole transport layer for high-performance polymer solar cells. *Org. Electron.* **44**, 176–182 (2017).
225. Capasso, A. *et al.* Chemical Vapor Deposited Graphene-Based Derivative As High-Performance Hole Transport Material for Organic Photovoltaics. *ACS Appl. Mater. Interfaces* **8**, 23844–23853 (2016).
226. Sarkar, A. S. *et al.* Facile embedding of gold nanostructures in the hole transporting layer for efficient polymer solar cells. *Org. Electron.* **54**, 148–153 (2018).
227. Iakobson, O. D. *et al.* Graphene nanosheet/polyaniline composite for transparent hole transporting layer. *J. Ind. Eng. Chem.* **65**, 309–317 (2018).
228. Abdulrazzaq, O. A., Bourdo, S. E., Saini, V. & Biris, A. S. Acid-free polyaniline:graphene-oxide hole transport layer in organic solar cells. *J. Mater. Sci. Mater. Electron.* **31**, 21640–21650 (2020).
229. Aatif, M. *et al.* Graphene oxide-molybdenum oxide composite with improved hole

- transport in bulk heterojunction solar cells. *AIP Adv.* **9**, 075215 (2019).
230. Cheng, J. *et al.* Self-Assembled Quasi-3D Nanocomposite: A Novel *p*-Type Hole Transport Layer for High Performance Inverted Organic Solar Cells. *Adv. Funct. Mater.* **28**, 1706403 (2018).
231. Dang, Y. *et al.* Solution processed hybrid Graphene-MoO₃ hole transport layers for improved performance of organic solar cells. *Org. Electron.* **67**, 95–100 (2019).
232. Christopholi, L. P. *et al.* Reduced graphene oxide and perylene derivative nanohybrid as multifunctional interlayer for organic solar cells. *Synth. Met.* **269**, 116552 (2020).
233. Lu, J., Yeo, P. S. E., Gan, C. K., Wu, P. & Loh, K. P. Transforming C₆₀ molecules into graphene quantum dots. *Nat. Nanotechnol.* **6**, 247–252 (2011).
234. Peng, J. *et al.* Graphene Quantum Dots Derived from Carbon Fibers. *Nano Lett.* **12**, 844–849 (2012).
235. Ho, N. T. *et al.* Solution-Processed Transparent Intermediate Layer for Organic Tandem Solar Cell Using Nitrogen-Doped Graphene Quantum Dots. *J. Nanosci. Nanotechnol.* **17**, 5686–5692 (2017).
236. Hoang, T. T., Pham, H. P. & Tran, Q. T. A Facile Microwave-Assisted Hydrothermal Synthesis of Graphene Quantum Dots for Organic Solar Cell Efficiency Improvement. *J. Nanomater.* **2020**, 1–8 (2020).
237. Zhang, X., Sun, S. & Liu, X. Amino functionalized carbon nanotubes as hole transport layer for high performance polymer solar cells. *Inorg. Chem. Commun.* **103**, 142–148 (2019).
238. Rajanna, P. M. *et al.* Rational design of highly efficient flexible and transparent *p*-type composite electrode based on single-walled carbon nanotubes. *Nano Energy* **67**, 104183 (2020).
239. Zhang, W. *et al.* Strongly enhanced efficiency of polymer solar cells through unzipped SWNT hybridization in the hole transport layer. *RSC Adv.* **10**, 24847–24854 (2020).